

Modal compression of the redshift-space galaxy bispectrum

Joyce Byun¹  and Elisabeth Krause¹

¹*Department of Astronomy and Steward Observatory, University of Arizona, 933 North Cherry Ave, Tucson, Arizona 85721, USA*

Accepted XXX. Received YYY; in original form ZZZ

ABSTRACT

We extend the modal decomposition method, previously applied to compress the information in the real-space bispectrum, to the anisotropic redshift-space galaxy bispectrum. In the modal method approach, the bispectrum is expanded on a basis of smooth functions of triangles and their orientations, such that a set of modal expansion coefficients can capture the information in the bispectrum. We assume a reference survey and compute Fisher forecasts for the compressed modal bispectrum and two other basis decompositions of the redshift-space bispectrum in the literature, one based on (single) spherical harmonics and another based on tripolar spherical harmonics. In each case, we compare the forecasted constraints from the compressed statistic with forecasted constraints from the full, uncompressed bispectrum which includes all triangles and orientations. Our main result is that all three compression methods achieve good recovery of the full information content of the bispectrum, but the modal decomposition approach achieves this the most efficiently: only 14 (42) modal expansion coefficients are necessary to obtain constraints that are within 10 (2) per cent of the full bispectrum result. The next most efficient decomposition is the one based on tripolar spherical harmonics, while the spherical harmonic multipoles are the least efficient.

Key words: Cosmology: theory – large-scale structure of the Universe.

1 INTRODUCTION

Large-scale galaxy surveys are able to place constraints on cosmological models by comparing the observed positions of galaxies with theoretical predictions, typically in the form of summary statistics describing the clustering properties of galaxies and matter. In a universe with nearly Gaussian initial conditions, most of the statistical information on galaxy clustering is captured by the two-point correlation function, or its Fourier transform, the power spectrum. However, due to non-linear gravitational clustering over time, higher-order statistics like the galaxy bispectrum, the Fourier transform of the three-point correlation function (3PCF), encode new complementary information on a wide range of science goals for upcoming galaxy surveys. Including the galaxy bispectrum in clustering analyses is expected to yield stronger constraints on galaxy bias and Λ CDM cosmological model parameters (Sefusatti et al. 2006; Song et al. 2015; Byun et al. 2017; Yankelevich & Porciani 2019; Gualdi & Verde 2020; Agarwal et al. 2021; Samushia et al. 2021; Oddo et al. 2021), primordial non-Gaussianity from inflation (Tellarini et al. 2016; Karagiannis et al. 2018; Moradinezhad Dizgah et al. 2021; Cabass et al. 2022a,b), neutrino physics (Ruggeri et al. 2018; Hahn et al. 2020; Hahn & Villaescusa-Navarro 2021; Yankelevich et al. 2022), modified gravity models (Yamauchi et al. 2017; Bose & Taruya 2018; Bose et al. 2020), and relativistic effects at the largest observable scales (Clarkson et al. 2019; Maartens et al. 2020; de Weerd et al. 2020; Maartens et al. 2021).

Currently, the strongest cosmological constraints from the galaxy bispectrum and 3PCF are from analyses of the SDSS BOSS survey (Gil-Marín et al. 2015a,b, 2017; Slepian et al. 2017; Gualdi et al. 2019b; Philcox & Ivanov 2022). While these analyses have included only the monopole component of the anisotropic bispectrum, higher bispectrum multipoles were detected by Sugiyama et al. (2019) and the (integrated) trispectrum was recently detected by Gualdi & Verde (2022). In the future, data from ongoing and future galaxy surveys, such as DESI, Euclid, and SPHEREx, will map the large-scale structure of the Universe in much larger volumes and with higher precision. In anticipation of these larger data sets, there is active development on many fronts to improve existing methods, and develop new approaches, for using the galaxy bispectrum as a cosmological observable.

For a standard likelihood-based analysis of galaxy clustering observables, a data covariance matrix is estimated from a large number of realistic mock catalogs generated at a fiducial cosmology. However, because the galaxy bispectrum is usually measured over a large number of data bins, obtaining accurate covariance matrices this way can be computationally very expensive. While one way to alleviate the computational burden is to develop techniques to run faster simulations that reduce the computational cost of generating mock catalogs (Colavincenzo et al. 2019), much effort has also been invested towards finding ways to avoid the brute-force approach to estimating covariance matrices. In principle,

* E-mail: joyce.byun@protonmail.com

it is possible to theoretically derive an accurate bispectrum covariance matrix and avoid the need for a large number of mocks. For example, the approach developed by [Wadekar & Scoccimarro \(2020\)](#) to calculate a theoretical covariance matrix for the galaxy power spectrum multipoles may also be promising for the bispectrum. Another possibility is to estimate the covariance matrix using fewer mocks, for example, by using a shrinkage estimator of the covariance ([Joachimi 2017](#)), fitting a model covariance ([Pearson & Samushia 2016](#)), creating a hybrid covariance matrix using both mocks and theoretical predictions ([Friedrich & Eifler 2018](#); [Hall & Taylor 2019](#)), or using a combination of fast approximate simulations and more expensive full N -body simulations ([Chartier & Wandelt 2021](#)).

Rather than developing methods for obtaining the covariance matrix, a different strategy is to pursue methods that compress the data vector, such that estimating the corresponding data covariance matrix requires fewer mock catalogs. This kind of approach can take different forms. One option is to explore alternative clustering observables that do not try to measure the bispectrum directly, but are still sensitive to higher-order correlations, including the bispectrum. Some examples of such observables are the line correlation function ([Obreschkow et al. 2013](#); [Wolstenhulme et al. 2015](#); [Eggemeier & Smith 2017](#); [Byun et al. 2017](#); [Franco et al. 2019](#); [Byun et al. 2020](#)), the integrated bispectrum ([Chiang et al. 2014, 2015](#); [Byun et al. 2017](#)), and skew spectra ([Pratten & Munshi 2012](#); [Schmittfull et al. 2015](#); [Moradinezhad Dizgah et al. 2020](#); [Dai et al. 2020](#); [Schmittfull & Moradinezhad Dizgah 2021](#)). The second option is to recover more directly the full cosmological information in the bispectrum through a compressed data set. A subset of these methods are general, in that they are not specific to bispectrum analyses, and can also be applied in other contexts, such as the galaxy power spectrum. These methods generally identify a small number of data bin combinations that contain most of the desired parameter information, and discard the rest of the data. For example, [Gualdi et al. \(2018, 2019b, 2020\)](#) compress the bispectrum monopole using the Karhunen-Loève/MOPED algorithm ([Tegmark et al. 1997](#); [Heavens et al. 2000](#); [Alsing & Wandelt 2018](#)), and subspace projection also appears to be a promising bispectrum compression method ([Philcox et al. 2021](#)). Other methods are specifically tailored to bispectrum analyses. For example, [Gualdi et al. \(2019a\)](#) compress the bispectrum by grouping similar triangles together. Another approach is to attempt to reconstruct the bispectrum through different basis expansions. The focus of this work is in this last category.

One of these methods is modal compression, which uses a well-chosen basis to reconstruct the bispectrum. First developed to search for primordial non-Gaussianity in the CMB ([Fergusson et al. 2010, 2012a](#); [Ade et al. 2014](#)), the method has been translated/adapted for LSS clustering ([Fergusson et al. 2012b](#); [Regan et al. 2012](#); [Schmittfull et al. 2013](#)) and has proven especially fruitful for studying the LSS bispectrum ([Lazanu et al. 2016, 2017](#); [Hung et al. 2019a,b](#)). Previous work on the real-space matter and halo bispectrum has shown that this method works very well to recover the equivalent constraints that we would get from measuring the standard bispectrum in many triangle bins ([Byun et al. 2017, 2021](#)).

In this work, we extend the modal bispectrum method from real-space to redshift-space, which is a necessary step for developing the modal method to be applied to real galaxy survey data. Along the way, we have compared it to two other bispectrum compression schemes in the literature, which rely on spherical harmonic ([Scoccimarro 2015](#); [Rizzo et al. 2022](#)) or tripolar spherical harmonic decompositions of the anisotropic bispectrum ([Sugiyama et al. 2019, 2020](#)). We approach these two other compression schemes as alternative basis expansions and compare their compression efficiency with the modal decomposition. We calculate Fisher forecasts on the parameters $(b_1, f, \sigma_8, \alpha_{\parallel}, \alpha_{\perp}, f_{\text{NL}})$. We find that all three compression schemes are able to recover the same forecasted constraints to within 10 per cent of the full anisotropic bispectrum, but the modal decomposition method achieves this the most efficiently, requiring only 32 modal expansion coefficients to achieve constraints that agree to within 2 per cent.

The outline of the rest of this paper is as follows. In Section 2, we review the theoretical modeling of the galaxy bispectrum using standard tree-level perturbation theory, and detail how we compute the benchmark Fisher forecast for the full anisotropic redshift-space galaxy bispectrum. In Sections 3 and 4, we review the bispectrum multipole decompositions based on spherical harmonics and tripolar spherical harmonics, respectively, and present their corresponding Fisher forecasts. In Section 5, we present the modal decomposition method for the redshift-space bispectrum and present a Fisher forecast. We conclude with a broader discussion of the main results in Section 6.

2 THE FULL INFORMATION CONTENT OF THE REDSHIFT-SPACE GALAXY BISPECTRUM

In this work, our aim is to compare different ways of recovering the cosmological information contained in the full anisotropic redshift-space bispectrum. Our benchmark is the maximum information content that can be recovered by measuring the full anisotropic bispectrum. We estimate this by computing a Fisher forecast that includes all possible triangle shapes and orientations, without using any compression scheme. The rest of this section provides the details of how we compute this benchmark Fisher forecast. We have modeled this forecast loosely on [Gagrani & Samushia \(2017\)](#) and our results support the results in this previous work, although the numerical implementation of our calculation is different and we adopt a different reference survey.

2.1 Modeling the galaxy power spectrum and bispectrum

To model the redshift-space galaxy power spectrum and bispectrum, we use the theoretical prediction from standard perturbation theory at tree-level (leading order) (Scoccimarro et al. 1999). Then the galaxy power spectrum and bispectrum are

$$P_g(\mathbf{k}) = Z_1^2(\mathbf{k})P_L(k) + P_{\text{SN}} \quad (1)$$

$$B_g(\mathbf{k}_1, \mathbf{k}_2, \mathbf{k}_3) = 2Z_2(\mathbf{k}_1, \mathbf{k}_2)Z_1(\mathbf{k}_1)Z_1(\mathbf{k}_2)P_L(k_1)P_L(k_2) + 2 \text{ perms.} + B_{\text{SN}}(\mathbf{k}_1, \mathbf{k}_2, \mathbf{k}_3) \quad (2)$$

where $\mathbf{k}_3 = -(\mathbf{k}_1 + \mathbf{k}_2)$, $P_L(k)$ is the linear matter power spectrum, and the first- and second-order redshift-space kernels are (Tellarini et al. 2016)

$$Z_1(\mathbf{k}_1) = (b_1 + f\mu_1^2) + \frac{f_{\text{NL}}b_\phi}{\mathcal{M}(k_1)} \quad (3)$$

$$\begin{aligned} Z_2(\mathbf{k}_1, \mathbf{k}_2) = & \frac{b_2}{2} + b_1 \left[F_2(\mathbf{k}_1, \mathbf{k}_2) + f_{\text{NL}} \frac{\mathcal{M}(k_3)}{\mathcal{M}(k_1)\mathcal{M}(k_2)} \right] + f\mu_3^2 \left[G_2(\mathbf{k}_1, \mathbf{k}_2) + f_{\text{NL}} \frac{\mathcal{M}(k_3)}{\mathcal{M}(k_1)\mathcal{M}(k_2)} \right] \\ & - \frac{f\mu_3k_3}{2} \left[\frac{\mu_1}{k_1} \left(b_1 + f\mu_2^2 + \frac{f_{\text{NL}}b_\phi}{\mathcal{M}(k_2)} \right) + \frac{\mu_2}{k_2} \left(b_1 + f\mu_1^2 + \frac{f_{\text{NL}}b_\phi}{\mathcal{M}(k_1)} \right) \right] \\ & + \frac{b_{s^2}}{2} \left(\mu_{12}^2 - \frac{1}{3} \right) + \frac{f_{\text{NL}}b_\phi\delta}{2} \left[\frac{1}{\mathcal{M}(k_1)} + \frac{1}{\mathcal{M}(k_2)} \right] + f_{\text{NL}}b_\phi \frac{\mu_{12}}{2} \left[\frac{k_2}{k_1} \frac{1}{\mathcal{M}(k_2)} + \frac{k_1}{k_2} \frac{1}{\mathcal{M}(k_1)} \right]. \end{aligned} \quad (4)$$

We have defined $\mu_i \equiv \hat{k}_i \cdot \hat{n}$ where \hat{n} is the line-of-sight direction and $\mu_{ij} \equiv \hat{k}_i \cdot \hat{k}_j$. F_2 and G_2 are the standard second-order density and velocity kernels (Bernardeau et al. 2002). f is the growth rate of structure, while f_{NL} is the amplitude of local-type primordial non-Gaussianity (PNG), and we only include terms that are necessary to describe terms in the power spectrum and bispectrum that are up to first-order in f_{NL} . b_1 , b_2 , and b_{s^2} are the linear, quadratic, and non-local galaxy bias parameters, respectively, while b_ϕ and $b_{\phi\delta}$ are two additional PNG galaxy bias parameters. In this work, we simplify the modeling of galaxy bias by assuming that galaxy bias is local in Lagrangian space, leading to $b_{s^2} = -\frac{4}{7}(b_1 - 1)$ (Chan et al. 2012; Baldauf et al. 2012; Saito et al. 2014). We also assume that the universality relations hold, such that $b_\phi = 2\delta_c(b_1 - 1)$ and $b_{\phi\delta} = b_\phi - b_1 + 1 + \delta_c[b_2 - \frac{8}{21}(b_1 - 1)]$ (see Moradinezhad Dizgah et al. (2020); Barreira (2021) and the references therein for discussions of the universal mass function assumption). $\mathcal{M}(k) \equiv 2k^2T(k)/3\Omega_m H_0^2$, where $T(k)$ is the matter transfer function, relates the linear density fluctuation at late times to the primordial Bardeen potential, $\delta(k) = \mathcal{M}(k)\phi(k)$.

The shot noise contributions are

$$P_{\text{SN}} = \frac{1}{n_g} \quad (5)$$

$$B_{\text{SN}}(\mathbf{k}_1, \mathbf{k}_2, \mathbf{k}_3) = \frac{1}{n_g} \left[Z_1^2(\mathbf{k}_1)P_L(k_1) + 2 \text{ perms.} \right] + \frac{1}{n_g^2} \quad (6)$$

where n_g is the average galaxy number density.

In addition to the dynamical redshift-space distortions that are described by the tree-level perturbation theory predictions above, the observed power spectrum and bispectrum are also subject to geometric distortions due to the Alcock-Paczynski (AP) effect (Alcock & Paczynski 1979). If the assumed cosmology used to translate redshifts and angles into distances and positions differs from the true cosmology, there will be additional distortions parallel and perpendicular to the line of sight. These geometric distortions can in turn provide clues to the true cosmology. Here we parametrize the AP effect using two parameters, α_\parallel and α_\perp , that distort wave-vectors differently parallel and perpendicular to the line of sight, $\mathbf{q}_i = \mathbf{k}_{i\parallel}/\alpha_\parallel + \mathbf{k}_{i\perp}/\alpha_\perp$, where the \mathbf{k}_i (\mathbf{q}_i) to correspond to wave-vectors in the assumed (true) cosmology. Then the observed power spectrum and bispectrum are

$$P_g(\mathbf{k}) = \frac{P_g(\mathbf{q})}{\alpha_\perp^2 \alpha_\parallel} \quad (7)$$

$$B_g(\mathbf{k}_1, \mathbf{k}_2, \mathbf{k}_3) = \frac{B_g(\mathbf{q}_1, \mathbf{q}_2, \mathbf{q}_3)}{(\alpha_\perp^2 \alpha_\parallel)^2}. \quad (8)$$

In practice, this means we use the same models for P_g and B_g as in eqs. (1) and (2), but evaluate the wavenumber arguments after AP rescaling, and normalize the power spectrum and bispectrum amplitudes by $\alpha_\perp^2 \alpha_\parallel$ and $(\alpha_\perp^2 \alpha_\parallel)^2$, respectively.

The tree-level perturbation theory modeling that we have summarised here is valid on large scales, while higher-order (loop) contributions and phenomenological Finger-of-God damping factors are often employed to improve the modeling on smaller, more non-linear scales. In this work, we do not go beyond the tree-level model in eqs. (1) and (2). While we do not anticipate that more advanced modeling of non-linearities will have a large impact on the relative comparisons between bispectrum estimators, we leave it to future work to explore the impact of non-linearities on the comparison between estimators.

2.2 Benchmark forecast

In the benchmark forecast, we calculate a Fisher matrix for the unrealistic scenario where we could measure the galaxy bispectrum for all Fourier-space triangles and orientations without any compression scheme.

If $\delta(\mathbf{k})$ is the Fourier transform of the galaxy density contrast field, then it is useful to define the quantity

$$\hat{\mathcal{B}}(\mathbf{k}_1, \mathbf{k}_2, \mathbf{k}_3) \equiv \frac{\delta(\mathbf{k}_1)\delta(\mathbf{k}_2)\delta(\mathbf{k}_3)}{V} \mathbb{1}_{\mathbf{k}_{123}} \quad (9)$$

where V is the surveyed volume and $\mathbb{1}_{\mathbf{k}_{123}}$ is equal to one if $\mathbf{k}_1 + \mathbf{k}_2 + \mathbf{k}_3 = 0$ and zero otherwise. Then $\hat{\mathcal{B}}$ is related to the theoretically predicted bispectrum through ensemble averaging, $\langle \hat{\mathcal{B}} \rangle = B_g$. The covariance of $\hat{\mathcal{B}}$ in the Gaussian limit is

$$\begin{aligned} \langle \hat{\mathcal{B}}(\mathbf{k}_1, \mathbf{k}_2, \mathbf{k}_3) \hat{\mathcal{B}}(\mathbf{k}'_1, \mathbf{k}'_2, \mathbf{k}'_3) \rangle = & \frac{(2\pi)^9}{V^2} P_g(\mathbf{k}_1) P_g(\mathbf{k}_2) P_g(\mathbf{k}_3) \left[\delta_D(\mathbf{k}_1 - \mathbf{k}'_1) \left(\delta_D(\mathbf{k}_2 - \mathbf{k}'_2) \delta_D(\mathbf{k}_3 - \mathbf{k}'_3) + \delta_D(\mathbf{k}_2 - \mathbf{k}'_3) \delta_D(\mathbf{k}_3 - \mathbf{k}'_2) \right) \right. \\ & + \delta_D(\mathbf{k}_1 - \mathbf{k}'_2) \left(\delta_D(\mathbf{k}_2 - \mathbf{k}'_3) \delta_D(\mathbf{k}_3 - \mathbf{k}'_1) + \delta_D(\mathbf{k}_2 - \mathbf{k}'_1) \delta_D(\mathbf{k}_3 - \mathbf{k}'_3) \right) \\ & \left. + \delta_D(\mathbf{k}_1 - \mathbf{k}'_3) \left(\delta_D(\mathbf{k}_2 - \mathbf{k}'_1) \delta_D(\mathbf{k}_3 - \mathbf{k}'_2) + \delta_D(\mathbf{k}_2 - \mathbf{k}'_2) \delta_D(\mathbf{k}_3 - \mathbf{k}'_1) \right) \right]. \quad (10) \end{aligned}$$

For the vast majority of closed triangles $(\mathbf{k}_1, \mathbf{k}_2, \mathbf{k}_3)$, the covariance will only be non-zero if $(\mathbf{k}'_1, \mathbf{k}'_2, \mathbf{k}'_3)$ describes the same triangle, and only one term out of the six terms on the right side of eq. (10) will be non-zero.¹ Because of this, we approximate the covariance as a diagonal matrix with

$$\langle \hat{\mathcal{B}}(\mathbf{k}_1, \mathbf{k}_2, \mathbf{k}_3) \hat{\mathcal{B}}(\mathbf{k}_1, \mathbf{k}_2, \mathbf{k}_3) \rangle = V P_g(\mathbf{k}_1) P_g(\mathbf{k}_2) P_g(\mathbf{k}_3). \quad (11)$$

In the continuous limit, the Fisher matrix for the set of parameters corresponding to θ_i is

$$\mathbf{F}_{ij} = \frac{V}{6} \int \frac{d^3 k_1}{(2\pi)^3} \int \frac{d^3 k_2}{(2\pi)^3} \int \frac{d^3 k_3}{(2\pi)^3} (2\pi)^3 \delta_D(\mathbf{k}_{123}) \frac{\partial B_g(\mathbf{k}_1, \mathbf{k}_2, \mathbf{k}_3)}{\partial \theta_i} \frac{1}{P_g(\mathbf{k}_1) P_g(\mathbf{k}_2) P_g(\mathbf{k}_3)} \frac{\partial B_g(\mathbf{k}_1, \mathbf{k}_2, \mathbf{k}_3)}{\partial \theta_j}. \quad (12)$$

In the last line, the factor of $1/6$ in front of the integrals is necessary because $B_g(\mathbf{k}_1, \mathbf{k}_2, \mathbf{k}_3)$ are equivalent under permutations of the three \mathbf{k}_i arguments and should not be counted as six separate measurements.

To all forecasts that are presented in this work, we include constraints from the full anisotropic power spectrum. The power spectrum Fisher matrix is

$$\mathbf{F}_{ij}^P = \frac{V}{2} \int \frac{d^3 k}{(2\pi)^3} \frac{\partial P_g(\mathbf{k})}{\partial \theta_i} \frac{1}{P_g(\mathbf{k})^2} \frac{\partial P_g(\mathbf{k})}{\partial \theta_j}. \quad (13)$$

Unless explicitly mentioned otherwise, the forecasts presented in this work do not directly use the continuous integration expressions shown above to compute the Fisher matrices. Instead, we compute discretized sums over the wave-vectors \mathbf{k}_i as determined by Fourier-space FFT grids by making the replacement

$$\int \frac{d^3 k}{(2\pi)^3} \rightarrow \frac{1}{V} \sum_{\mathbf{k}} \quad (14)$$

in eqs. (12) and (13).² For the bispectrum Fisher matrix in eq. (12), the discretized sum is computed efficiently if the partial derivative $\partial B_g / \partial \theta_i$ can be written as a function that is separable in its dependence on \mathbf{k}_1 , \mathbf{k}_2 , and \mathbf{k}_3 . This is made possible for the bispectrum model and Fisher parameters used in this work by using the modal basis functions that are presented later in Section 5.2.

2.3 Fisher forecast settings

In this work, our goal is to compare different ways of compressing information in the redshift-space galaxy bispectrum. For this purpose, we will compute Fisher forecasted constraints on $\theta = (b_1, b_2, f, \sigma_8, \alpha_\perp, \alpha_\parallel, f_{\text{NL}})$ for the full redshift-space bispectrum, the spherical harmonic $B_{\ell m}(k_1, k_2, k_3)$ multipoles (Scoccimarro 2015), the tripolar spherical harmonic (TriPoSH) $B_{\ell_1 \ell_2 L}(k_1, k_2)$ multipoles (Sugiyama et al. 2019), and the modal bispectrum coefficients β_n . Constraints from the full redshift-space bispectrum are the benchmark against which the other estimators are measured.

We will assume a reference survey of a single redshift slice with a volume, galaxy number density, and fiducial parameter values that are roughly similar to what will be included as one redshift bin in ongoing and upcoming spectroscopic galaxy surveys such as Euclid, DESI, and SPHEREx. More realistic forecasting for a specific survey scenario is outside the scope of this work. We expect that the forecasts here will still give us a reasonably accurate comparison between compression methods, although the absolute strength of the constraints will differ, but this should be checked for more realistic forecasts across different number densities.

We set our survey volume to be $V = 4.0 h^{-3} \text{ Gpc}^3$, which is approximately representative of a redshift shell at $z = 1$ with thickness $\Delta z = 0.1$ and a sky fraction of $f_{\text{sky}} = 0.35$. The galaxy number density is set to $n_g = 6 \times 10^{-4} h^3 \text{ Mpc}^{-3}$. This is similar to what is expected for the Euclid H α and DESI ELG samples at $z \sim 1$ (Blanchard et al. 2020; Aghamousa et al. 2016). SPHEREx plans to use five different tracers in each redshift bin (Doré et al. 2014), and this number density is roughly what is expected for the tracer with the highest number density.

We use the following cosmological parameter values to generate the linear matter power spectrum and matter transfer function at redshift

¹ For example, however, an exception to this would be a triangle where $\mathbf{k}_1 = \mathbf{k}_2$ and $\mathbf{k}_3 = -\mathbf{k}_1 - \mathbf{k}_2$. In this case, the first and fourth terms on the right side of eq. (10) would be non-zero.

² For FFT calculations in this work, we use the [Intel oneAPI Math Kernel Library](https://docs.intel.com/content/www/us/en/develop/oneapi-math-kernel-library.html).

$z = 1$ using CLASS³ (Blas et al. 2011): $\Omega_c = 0.2642$, $\Omega_b = 0.0493$, $H_0 = 67.4 \text{ km s}^{-1} \text{ Mpc}^{-1}$, $n_s = 0.965$, and $\sigma_8 = 0.811$. These parameters are consistent with constraints on the flat Λ CDM cosmological model from the Planck 2018 analysis of CMB temperature and polarization anisotropies and CMB lensing (Aghanim et al. 2020).

The fiducial values of the AP parameters are $\alpha_\perp = \alpha_\parallel = 1$, which corresponds to the assumption that the fiducial cosmology is the same as the true one. The fiducial value of f_{NL} is zero, as non-zero local PNG has yet to be detected. The fiducial bias parameters are $b_1 = 1.50$ and for b_2 we use the fitting formula for quadratic bias in Lazeyras et al. (2016), $b_2 = 0.412 - 2.143 b_1 + 0.929 b_1^2 + 0.008 b_1^3$.

3 SPHERICAL HARMONIC DECOMPOSITION

In this section, we review the spherical harmonic multipole decomposition from Scoccimarro (2015), compute Fisher forecasts for the $B_{\ell m}$ multipoles, and compare the constraints from $B_{\ell m}$ to the benchmark forecast. The work in this section obtains results that are similar to Gagrani & Samushia (2017).

3.1 Definition of $B_{\ell m}$ multipoles

The redshift-space bispectrum is a function that depends on the shape of the triangle that is formed by (k_1, k_2, k_3) , as well as the relative orientation between this triangle and the line of sight, which can be parametrized with two angles. The $B_{\ell m}$ multipoles decompose this dependence on triangle orientation into spherical harmonics,

$$B_{\ell m}(k_1, k_2, k_3) = \int \frac{d^2 \hat{n}}{4\pi} B(\mathbf{k}_1, \mathbf{k}_2, \hat{n}) Y_{\ell m}^*(\theta, \phi), \quad (15)$$

where the angles (θ, ϕ) correspond to the polar and azimuthal angles describing the line of sight direction \hat{n} in a coordinate system determined by \hat{k}_1 and \hat{k}_2 , such that \hat{k}_1 defines the z -axis and \hat{k}_2 lies in the xz -plane. We choose the $Y_{\ell m}$ to be normalized such that $Y_{00} = 1$ and

$$\int \frac{d^2 \hat{n}}{4\pi} Y_{\ell m}(\hat{n}) Y_{\ell' m'}^*(\hat{n}) = \delta_{\ell \ell'}^K \delta_{m m'}^K. \quad (16)$$

Since the $B_{\ell m}$ are the multipoles for a real-valued quantity, the multipoles with $m = 0$ will be real-valued, and the multipoles with $m \neq 0$ will be complex-valued. The multipoles for $m < 0$ are then $B_{\ell}^{-|m|} = (-1)^{|m|} B_{\ell}^{|m|*}$, so we only keep the unique multipoles with $m \geq 0$.

3.2 $\hat{B}_{\ell m}$ estimator and covariance

In the global plane-parallel limit, where the line of sight over the survey volume is fixed to \hat{z} , the estimator is

$$\hat{B}_{\ell m}(k_1, k_2, k_3) = \frac{1}{N_{\text{tri}}} \int_{k_1} \frac{d^3 q_1}{(2\pi)^3} \int_{k_2} \frac{d^3 q_2}{(2\pi)^3} \int_{k_3} \frac{d^3 q_3}{(2\pi)^3} (2\pi)^3 \delta_D(\mathbf{q}_{123}) \hat{\mathcal{B}}(\mathbf{q}_1, \mathbf{q}_2, \mathbf{q}_3) Y_{\ell m}^*(\theta, \phi), \quad (17)$$

where the normalization factor is

$$N_{\text{tri}} = \int_{k_1} \frac{d^3 q_1}{(2\pi)^3} \int_{k_2} \frac{d^3 q_2}{(2\pi)^3} \int_{k_3} \frac{d^3 q_3}{(2\pi)^3} (2\pi)^3 \delta_D(\mathbf{q}_{123}). \quad (18)$$

The subscript on the integral, \int_{k_i} , is shorthand for indicating that the integral is only over the Fourier-space shell centered at k_i .

Then the covariance is

$$\begin{aligned} & \langle \hat{B}_{\ell m}(k_1, k_2, k_3) \hat{B}_{\ell' m'}^*(k'_1, k'_2, k'_3) \rangle \\ &= \frac{1}{N_{\text{tri}} N'_{\text{tri}}} \int_{k_1} \frac{d^3 q_1}{(2\pi)^3} \int_{k_2} \frac{d^3 q_2}{(2\pi)^3} \int_{k_3} \frac{d^3 q_3}{(2\pi)^3} (2\pi)^3 \delta_D(\mathbf{q}_{123}) \int_{k'_1} \frac{d^3 q'_1}{(2\pi)^3} \int_{k'_2} \frac{d^3 q'_2}{(2\pi)^3} \int_{k'_3} \frac{d^3 q'_3}{(2\pi)^3} (2\pi)^3 \delta_D(\mathbf{q}'_{123}) \\ & \quad \times \langle \hat{\mathcal{B}}(\mathbf{q}_1, \mathbf{q}_2, \mathbf{q}_3) \hat{\mathcal{B}}(\mathbf{q}'_1, \mathbf{q}'_2, \mathbf{q}'_3) \rangle Y_{\ell m}^*(\theta, \phi) Y_{\ell' m'}(\theta', \phi') \\ &= \delta_{k_1 k'_1}^K \delta_{k_2 k'_2}^K \delta_{k_3 k'_3}^K \frac{s_\Delta}{N_{\text{tri}}^2 V} \int_{k_1} \frac{d^3 q_1}{(2\pi)^3} \int_{k_2} \frac{d^3 q_2}{(2\pi)^3} \int_{k_3} \frac{d^3 q_3}{(2\pi)^3} (2\pi)^3 \delta_D(\mathbf{q}_{123}) P_g(\mathbf{q}_1) P_g(\mathbf{q}_2) P_g(\mathbf{q}_3) Y_{\ell m}^*(\theta, \phi) Y_{\ell' m'}(\theta, \phi) \end{aligned} \quad (19)$$

where we have used eq. (10) for $\langle \hat{\mathcal{B}} \hat{\mathcal{B}}' \rangle$. The three Kronecker delta factors emphasize that the covariance is only non-zero if the two triangle bins are the same, $k_1 = k'_1$, $k_2 = k'_2$, and $k_3 = k'_3$. We note however that generally there is a non-zero covariance between multipoles with different (ℓ, m) . s_Δ is a factor that depends on whether the triangle bin is equilateral ($s_\Delta = 6$), isosceles ($s_\Delta = 2$), or scalene ($s_\Delta = 1$).

We can simplify this six-dimensional integral expression for the covariance by taking the thin-shell approximation. Assuming that the width of each k_i bin is small enough that we can safely replace the magnitudes of the \mathbf{q}_i wave-vectors in the integrand with k_i , we can exchange the integral over all triangle orientations for a two-dimensional integral over all \hat{n} directions,

$$\langle \hat{B}_{\ell m}(k_1, k_2, k_3) \hat{B}_{\ell' m'}^*(k_1, k_2, k_3) \rangle = \frac{s_\Delta}{N_{\text{tri}} V} \int \frac{d^2 \hat{n}}{4\pi} P_g(k_1) P_g(k_2) P_g(k_3) Y_{\ell m}^*(\theta, \phi) Y_{\ell' m'}(\theta, \phi). \quad (20)$$

³ <http://class-code.net>

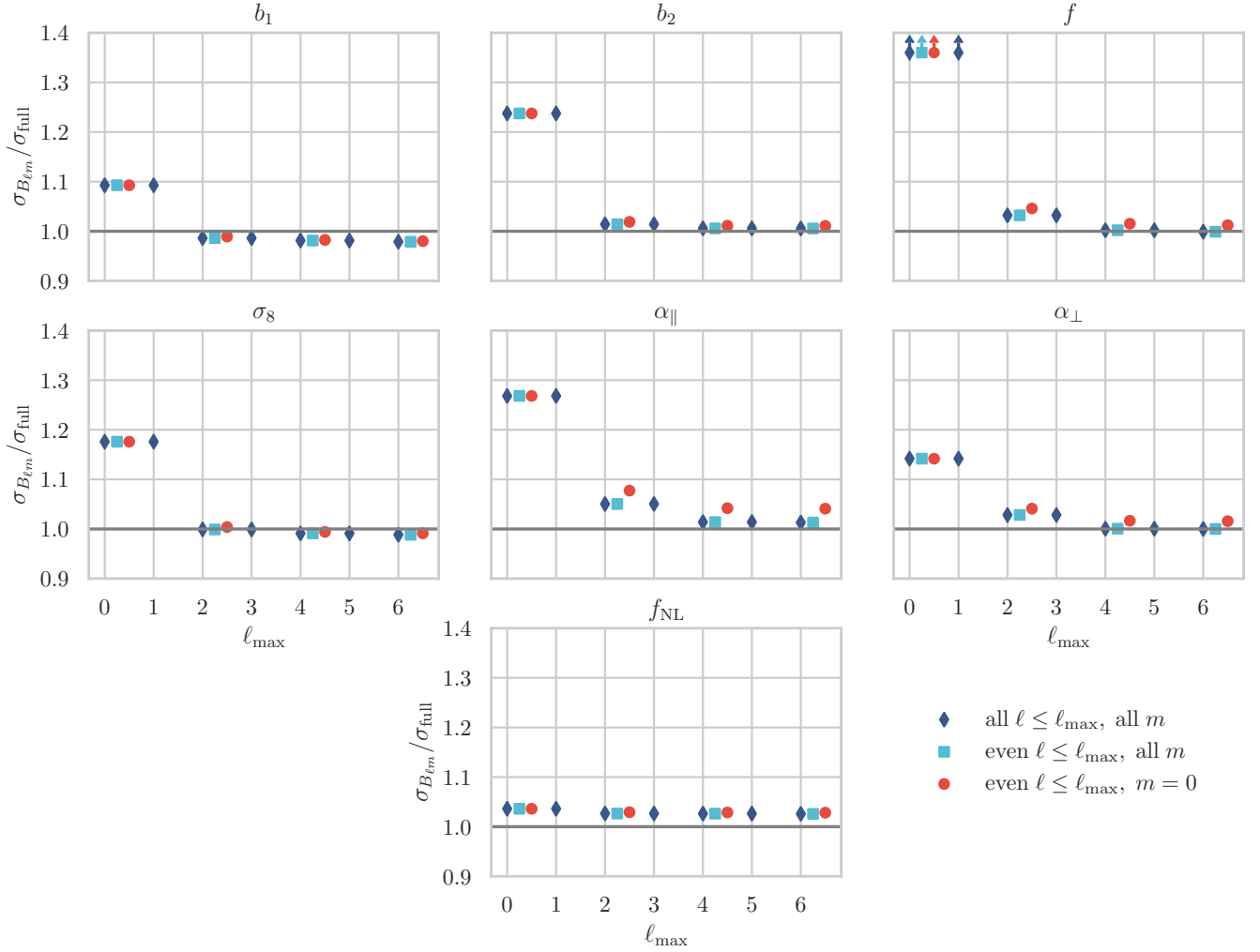


Figure 1. Ratio of constraints from $B_{\ell m}$ and the full redshift-space bispectrum, $\sigma_{B_{\ell m}}/\sigma_{full}$, as a function of including $B_{\ell m}$ multipoles up to ℓ_{max} for parameters ($b_1, b_2, f, \sigma_8, \alpha_{||}, \alpha_{\perp}, f_{NL}$). We note that for the parameters b_1 and σ_8 in the first column of panels, the forecasted error from the $B_{\ell m}$ multipoles can be up to 3 per cent *smaller* than what is forecasted from the full bispectrum, due to the thin-shell approximation. We find that the odd ℓ multipoles (included in the dark blue diamonds) do not contribute any additional information, and constraints show negligible improvement by the inclusion of $\ell = 6$ multipoles. Only a small amount of information is lost by leaving out the $m \neq 0$ multipoles, as shown by the difference between light blue squares and red circles. Constraints up to $\ell_{max} = 4$ including all $m \geq 0$ multipoles are within 3 per cent of the full bispectrum constraint. This increases very slightly to 5 per cent when the non-zero m multipoles are dropped. This latter case including the multipoles (B_{00}, B_{20}, B_{40}) corresponds to a data vector with 1,197 bins.

The bispectrum multipole estimator in eq. (17) is usually a computationally infeasible six-dimensional integral over the FFT grids for \mathbf{q}_1 and \mathbf{q}_2 . Scoccimarro (2015) has noted that this calculation for the $m = 0$ multipoles can be computed easily, since $Y_{\ell 0}(\theta, \phi)$ reduces to a Legendre polynomial that only depends on the angle between \mathbf{q}_1 and the line of sight, $Y_{\ell 0}(\theta, \phi) = \mathcal{L}_{\ell}(\cos \theta_1)$, and the Dirac delta function can also be written in a separable way as

$$\delta_D(\mathbf{q}_{123}) = \int \frac{d^3 x}{(2\pi)^3} e^{i(\mathbf{q}_1 + \mathbf{q}_2 + \mathbf{q}_3) \cdot \mathbf{x}}. \quad (21)$$

Then the estimator for $\hat{B}_{\ell 0}$ can be computed efficiently as

$$\hat{B}_{\ell 0}(k_1, k_2, k_3) = \frac{1}{N_{\text{tri}} V} \int d^3 x \left[\int_{k_1} \frac{d^3 q_1}{(2\pi)^3} e^{i\mathbf{q}_1 \cdot \mathbf{x}} \delta(\mathbf{q}_1) \mathcal{L}_{\ell}(\cos \theta_1) \right] \left[\int_{k_2} \frac{d^3 q_2}{(2\pi)^3} e^{i\mathbf{q}_2 \cdot \mathbf{x}} \delta(\mathbf{q}_2) \right] \left[\int_{k_3} \frac{d^3 q_3}{(2\pi)^3} e^{i\mathbf{q}_3 \cdot \mathbf{x}} \delta(\mathbf{q}_3) \right]. \quad (22)$$

However, for the $m \neq 0$ multipoles, it is not clear whether the estimator can be cast into a similarly separable form. In the forecasted results that follow, we therefore consider two scenarios: one where only the $B_{\ell 0}$ multipoles are included and another where all $B_{\ell m}$ multipoles are included.

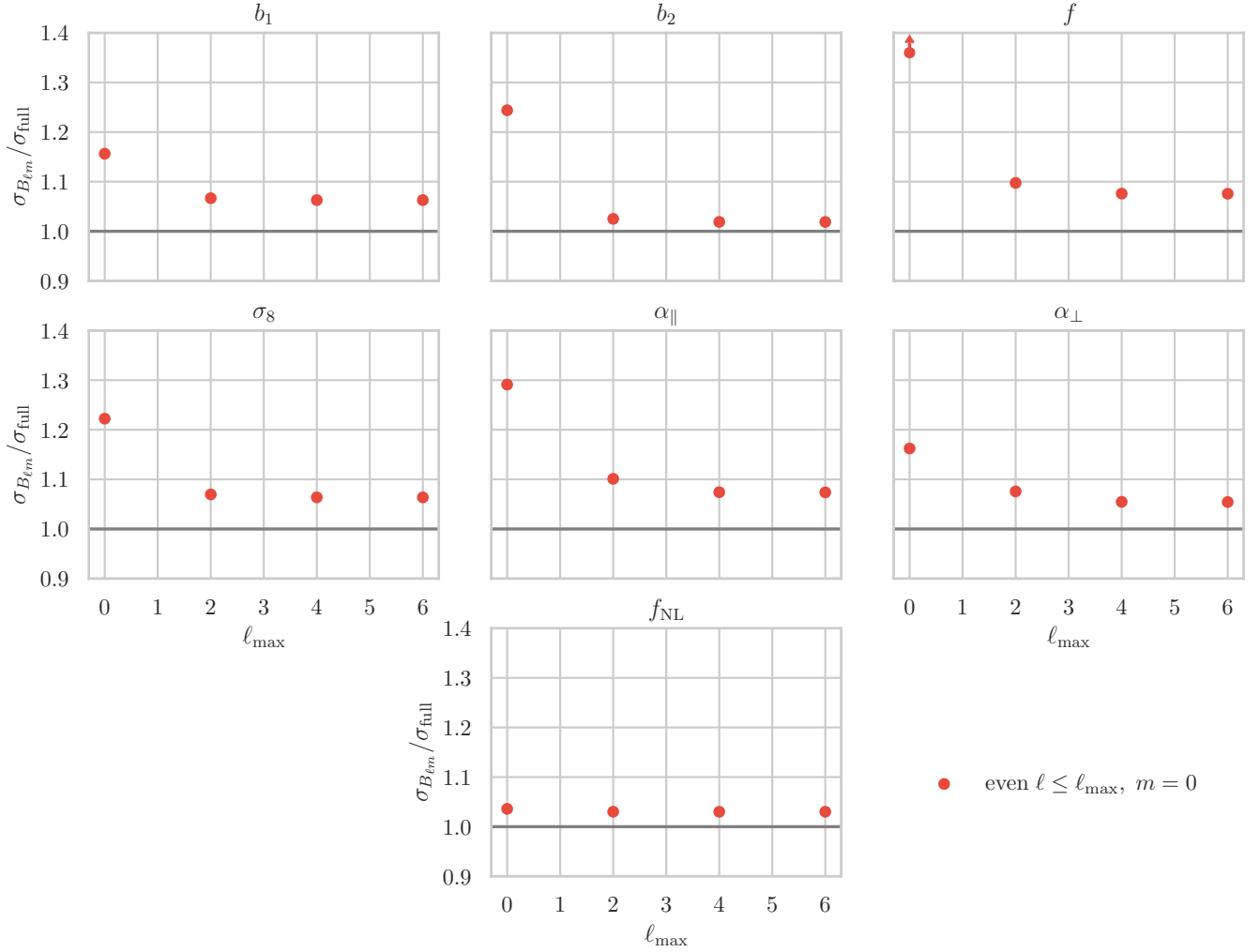


Figure 2. The same as Fig. 1, except we consider here only the $B_{\ell m}$ multipoles with even ℓ and $m = 0$ and compute the Fisher matrices using FFT-based expressions that do not assume the thin-shell approximation for $B_{\ell m}$ and its covariance. We find that constraints converge with $\ell_{\text{max}} = 4$ as in Fig. 1, but the agreement between the $B_{\ell 0}$ forecast and the full bispectrum constraint loosens slightly from the 5 per cent in Fig. 1 to 8 per cent here.

3.3 $B_{\ell m}$ Fisher forecast results

The Fisher matrix for $B_{\ell m}$ is

$$\mathbf{F}_{ij} \equiv \sum_{\ell m} \sum_{\ell' m'} \sum_{k_1 k_2 k_3} \frac{\partial B_{\ell m}(k_1, k_2, k_3)}{\partial \theta_i} \mathbf{C}^{-1} [B_{\ell m}(k_1, k_2, k_3), B_{\ell' m'}^*(k_1, k_2, k_3)] \frac{\partial B_{\ell' m'}^*(k_1, k_2, k_3)}{\partial \theta_j} + \mathbf{F}_{ij}^P. \quad (23)$$

The (k_1, k_2, k_3) triangle bins are determined by the center of the lowest k -bin, $k_{\text{min}} = 0.02 h \text{ Mpc}^{-1}$, the center of the highest k -bin, $k_{\text{max}} = 0.15 h \text{ Mpc}^{-1}$, and the bin width $\Delta k = 0.01 h \text{ Mpc}^{-1}$. We only include unique triangle bins by requiring that $k_1 \geq k_2 \geq k_3$. In total there are 399 triangle bins per multipole.

Using the continuous integral expressions in eq. (15) to compute the derivatives and eq. (20) to compute the covariance,⁴ we obtain the Fisher forecasted errors $\sigma_{B_{\ell m}}$ on the parameters $(b_1, b_2, f, \sigma_8, \alpha_{\parallel}, \alpha_{\perp}, f_{\text{NL}})$. The errors σ_{full} from the full redshift-space bispectrum are computed by evaluating eq. (12) as continuous integrals using the CUBA library (Hahn 2005, 2015).⁵ The ratios between $\sigma_{B_{\ell m}}$ and σ_{full} are shown in Fig. 1 for different combinations of multipoles, indicated by three different marker symbols. We note that in the first column of Fig. 1, we find that for b_1 and σ_8 , $\sigma_{B_{\ell m}}$ can be up to 3 per cent *smaller* than σ_{full} , which is an unphysical numerical artifact due to the use of the thin-shell approximation in the estimator and covariance expressions in eqs. (15) and (20). We have checked that wider bin widths Δk exacerbate this

⁴ We used the SHTOOLS library (Wieczorek & Meschede 2018) available at <https://github.com/SHTOOLS/SHTOOLS>.

⁵ <http://www.feynarts.de/cuba/>

discrepancy, while smaller bin widths make the difference smaller, at the cost of rapidly increasing the total number of triangle bins in the forecast.

We identify broad trends in the forecasted constraints that agree with the results in [Gagrani & Samushia \(2017\)](#). We find that the odd ℓ multipoles (included in the points marked by dark blue diamonds) add negligible constraining power. Including even ℓ multipoles up to $\ell_{\max} = 4$ (as shown by the light blue squares) recovers most of the available information, with constraints on all parameters within 3 per cent of the constraints from the full bispectrum forecast. If only the $m = 0$ multipoles are used (red circles), the constraints are also saturated at $\ell_{\max} = 4$, but a small amount of information is lost. This is most noticeable for α_{\parallel} , where the error is 5 per cent larger than from the full bispectrum. This combination of multipoles, B_{00} , B_{20} , and B_{40} , corresponds to a data vector with $399 \times 3 = 1,197$ bins.

For this last scenario marked by the red circles, including only $B_{\ell 0}$ for even ℓ , we are able to calculate the Fisher derivatives and covariance matrix using the FFT-based expressions in eqs. (19) and (22). Similarly, we compute the full bispectrum forecast in eq. (12) using FFTs. The comparison of FFT-based forecasts is shown in Fig. 2, and we consider this comparison to be more accurate, since it does not use the thin-shell approximation when computing $B_{\ell m}$ and its covariance. We find that the $B_{\ell 0}$ for $\ell = 0, 2$, and 4 can recover parameter constraints to within 8 per cent of the full bispectrum.

4 TRIPOLAR SPHERICAL HARMONIC DECOMPOSITION

In this section, we focus on a second, different decomposition of the redshift-space bispectrum that uses a basis of tripolar spherical harmonic (TripoSH) functions ([Varshalovich et al. 1988](#)) rather than (single) spherical harmonics. We briefly review the TripoSH decomposition of the bispectrum presented in [Sugiyama et al. \(2019, 2020\)](#), including its estimator and covariance, before presenting the Fisher forecast for the TripoSH $B_{\ell_1 \ell_2 L}$ multipoles compared to the full redshift-space bispectrum. To our knowledge, this is the first such comparison in the literature.

We note that the TripoSH basis for the bispectrum is related to many previous works that used bipolar or tripolar spherical harmonics to study the CMB and large-scale structure. For example, bipolar spherical harmonics were first proposed by [Hajian & Souradeep \(2003, 2005\)](#) to study the statistical isotropy of the CMB and has been used by the Planck collaboration to put constraints on deviations from statistical isotropy ([Ade et al. 2016](#)). For large-scale structure studies, the bipolar spherical harmonics formalism has been used to constrain statistical anisotropy in the galaxy power spectrum ([Shiraishi et al. 2017; Sugiyama et al. 2018](#)) and tripolar spherical harmonics have also been used to capture wide-angle effects in the two-point correlation function ([Szapudi 2004](#)).

4.1 Definition of TripoSH multipoles

[Sugiyama et al. \(2019\)](#) presented an alternative way to decompose the anisotropic bispectrum using a tripolar spherical harmonic (TripoSH) basis. The TripoSH basis is a tensor product of three spherical harmonics, $\{Y_{\ell_1}(\hat{k}_1) \otimes Y_{\ell_2}(\hat{k}_2)\}_{\ell_{12}} \otimes Y_L(\hat{n})\}_{JM_J}$, that can be used to describe how the bispectrum depends on three directions, \hat{k}_1 , \hat{k}_2 and \hat{n} . The advantage of using this basis is that the TripoSH basis functions have many of the same properties as spherical harmonics: they obey similar orthogonality conditions, rotate like spherical harmonics, and behave similarly under coordinate inversions ([Varshalovich et al. 1988](#)). These properties can be used to relate cosmological assumptions to restrictions on the allowed multipole coefficients, which in general would be the full set of $B_{\ell_1 \ell_2 \ell_{12} L}^{JM_J}(k_1, k_2)$ multipole coefficients. Assuming that the bispectrum is statistically isotropic translates to requiring that $J = M_J = 0$ for the total angular momenta, and it follows that then the only non-zero multipoles are those with $\ell_{12} = L$. Assuming that the universe is parity symmetric is equivalent to having only the $\ell_1 + \ell_2 + L = \text{even}$ multipoles be non-zero.

Under typical assumptions of a homogeneous, isotropic, and parity-symmetric universe then, the bispectrum can be expanded on the TripoSH basis as

$$B(\mathbf{k}_1, \mathbf{k}_2, \hat{n}) = \sum_{\ell_1 + \ell_2 + L = \text{even}} B_{\ell_1 \ell_2 L}(k_1, k_2) S_{\ell_1 \ell_2 L}(\hat{k}_1, \hat{k}_2, \hat{n}), \quad (24)$$

where the TripoSH basis functions are

$$S_{\ell_1 \ell_2 L}(\hat{k}_1, \hat{k}_2, \hat{n}) = \frac{1}{H_{\ell_1 \ell_2 L}} \sum_{m_1 m_2 M} \begin{pmatrix} \ell_1 & \ell_2 & L \\ m_1 & m_2 & M \end{pmatrix} \mathcal{Y}_{\ell_1}^{m_1}(\hat{k}_1) \mathcal{Y}_{\ell_2}^{m_2}(\hat{k}_2) \mathcal{Y}_L^M(\hat{n}) \quad (25)$$

and the TriPoSH multipoles are

$$B_{\ell_1 \ell_2 L}(k_1, k_2) = H_{\ell_1 \ell_2 L} \sum_{m_1 m_2 M} \begin{pmatrix} \ell_1 & \ell_2 & L \\ m_1 & m_2 & M \end{pmatrix} B_{\ell_1 \ell_2 L}^{m_1 m_2 M}(k_1, k_2) \quad (26)$$

$$B_{\ell_1 \ell_2 L}^{m_1 m_2 M}(k_1, k_2) \equiv N_{\ell_1 \ell_2 L} \int \frac{d^2 k_1}{4\pi} \int \frac{d^2 k_2}{4\pi} \int \frac{d^2 \hat{n}}{4\pi} \mathcal{Y}_{\ell_1}^{m_1*}(\hat{k}_1) \mathcal{Y}_{\ell_2}^{m_2*}(\hat{k}_2) \mathcal{Y}_L^M(\hat{n}) B(\mathbf{k}_1, \mathbf{k}_2, \hat{n}). \quad (27)$$

The Wigner 3- j symbols require that (ℓ_1, ℓ_2, L) combinations satisfy the triangle inequality, $|\ell_1 - \ell_2| \leq L \leq \ell_1 + \ell_2$. We use the same notations as in [Sugiyama et al. \(2019\)](#) and define the factors $H_{\ell_1 \ell_2 L} \equiv \begin{pmatrix} \ell_1 & \ell_2 & L \\ 0 & 0 & 0 \end{pmatrix}$, which acts to only select multipoles that have $\ell_1 + \ell_2 + L = \text{even}$, and $N_{\ell_1 \ell_2 L} \equiv (2\ell_1 + 1)(2\ell_2 + 1)(2L + 1)$. To match that work, we note that here we are using spherical harmonics that are normalized

differently to the ones in Section 3. The $Y_{\ell m}$ spherical harmonics in eq. (16) are 4π normalized, while the ones we use in this section are Schmidt semi-normalized, $\mathcal{Y}_{\ell m} = Y_{\ell m}/\sqrt{2\ell+1}$, so that $\int d\Omega \mathcal{Y}_{\ell m} \mathcal{Y}_{\ell' m'}^* = 4\pi/(2\ell+1)\delta_{\ell\ell'}\delta_{mm'}$.

The $L = 0$ multipoles, $B_{\ell_1\ell_20}(k_1, k_2)$, describe the bispectrum monopole, while the $L > 0$ multipoles can only be non-zero in the presence of anisotropic RSD or AP effects. We do not consider multipoles with odd L ; while it is not immediately obvious that odd L multipoles carry negligible information, our results will show that very little constraining power is lost by including only the even L multipoles. Since parity symmetry requires $\ell_1 + \ell_2 + L = \text{even}$, if L is even it follows that $\ell_1 + \ell_2$ is also even. For these combinations of (ℓ_1, ℓ_2, L) , the $B_{\ell_1\ell_2L}$ multipoles are real-valued.

In this work, we make the global plane-parallel approximation so that the line-of-sight direction is fixed and determines the \hat{z} -axis for the spherical harmonic functions. Since $\mathcal{Y}_{LM}(\hat{z}) = \delta_{M0}^K$, this simplifies the expressions for the TriPoSH multipoles in eqs. (26) and (27) to

$$B_{\ell_1\ell_2L}(k_1, k_2) = H_{\ell_1\ell_2L} \sum_m \begin{pmatrix} \ell_1 & \ell_2 & L \\ m & -m & 0 \end{pmatrix} B_{\ell_1\ell_2L}^{m-m_0}(k_1, k_2) \quad (28)$$

$$B_{\ell_1\ell_2L}^{m-m_0}(k_1, k_2) = N_{\ell_1\ell_2L} \int \frac{d^2\hat{k}_1}{4\pi} \int \frac{d^2\hat{k}_2}{4\pi} \mathcal{Y}_{\ell_1}^{m*}(\hat{k}_1) \mathcal{Y}_{\ell_2}^{-m*}(\hat{k}_2) B(\mathbf{k}_1, \mathbf{k}_2) \mathbb{1}(k_3). \quad (29)$$

In the last equation, we have added the factor $\mathbb{1}(k_3)$ to the integrand. It is defined such that $\mathbb{1}(k_3) = 1$ if k_3 falls into the allowed (k_{\min}, k_{\max}) range and zero otherwise. In Sugiyama et al. (2019), the integral above is over all triangles where two of the legs are (k_1, k_2) . Therefore, if k_1 and k_2 can go as high as k_{\max} , then the allowed range of k_3 will go up to $2k_{\max}$. However, this range of allowed triangles is different to the range of triangles that were used in the previous Fisher forecasts for the full bispectrum and $B_{\ell m}$ in Section 3, where each leg of the triangle had to be in the same k range, $k_{\min} \leq k_1, k_2, k_3 \leq k_{\max}$. To make the forecasts cover the same k range, we modify the integrals over \hat{k}_1 and \hat{k}_2 to impose the same (k_{\min}, k_{\max}) limits on k_3 :

$$\int \frac{d^2\hat{k}_1}{4\pi} \int \frac{d^2\hat{k}_2}{4\pi} \rightarrow \int \frac{d^2\hat{k}_1}{4\pi} \int \frac{d^2\hat{k}_2}{4\pi} \mathbb{1}(k_3). \quad (30)$$

4.2 $\hat{B}_{\ell_1\ell_2L}$ estimator and covariance

In the global plane-parallel limit, the estimator for $B_{\ell_1\ell_2L}$ takes the same form as eq. (28) where the estimator for $B_{\ell_1\ell_2L}^{m-m_0}(k_1, k_2)$ is

$$\begin{aligned} \hat{B}_{\ell_1\ell_2L}^{m_1m_20}(k_1, k_2) &= N_{\ell_1\ell_2L} \int \frac{d^2\hat{k}_1}{4\pi} \mathcal{Y}_{\ell_1}^{m_1*}(\hat{k}_1) \int \frac{d^2\hat{k}_2}{4\pi} \mathcal{Y}_{\ell_2}^{m_2*}(\hat{k}_2) \int d^3k_3 \delta_D(\mathbf{k}_{123}) \hat{\mathcal{B}}(\mathbf{k}_1, \mathbf{k}_2, \mathbf{k}_3) \mathbb{1}(k_3) \\ &= \frac{N_{\ell_1\ell_2L}}{N_{\text{modes}}(k_1, k_2)} \int_{k_1} \frac{d^3q_1}{(2\pi)^3} \mathcal{Y}_{\ell_1}^{m_1*}(\hat{q}_1) \int_{k_2} \frac{d^3q_2}{(2\pi)^3} \mathcal{Y}_{\ell_2}^{m_2*}(\hat{q}_2) \int \frac{d^3q_3}{(2\pi)^3} (2\pi)^3 \delta_D(\mathbf{q}_{123}) \hat{\mathcal{B}}(\mathbf{q}_1, \mathbf{q}_2, \mathbf{q}_3) \mathbb{1}(q_3). \end{aligned} \quad (31)$$

In the second line we have exchanged the integrals over \hat{k}_1 and \hat{k}_2 for integrals over \mathbf{q}_1 and \mathbf{q}_2 in 3-dimensional Fourier-space shells and defined

$$N_{\text{modes}}(k_1, k_2) \equiv \int_{k_1} \frac{d^3q_1}{(2\pi)^3} \int_{k_2} \frac{d^3q_2}{(2\pi)^3} \mathbb{1}(q_3). \quad (32)$$

Then the covariance for the TriPoSH multipoles is

$$\begin{aligned} \langle \hat{B}_{\ell_1\ell_2L}(k_1, k_2) \hat{B}_{\ell'_1\ell'_2L'}(k'_1, k'_2) \rangle &= H_{\ell_1\ell_2L} H_{\ell'_1\ell'_2L'} \sum_m \begin{pmatrix} \ell_1 & \ell_2 & L \\ m & -m & 0 \end{pmatrix} \sum_{m'} \begin{pmatrix} \ell'_1 & \ell'_2 & L' \\ m' & -m' & 0 \end{pmatrix} \langle \hat{B}_{\ell_1\ell_2L}^{m-m_0}(k_1, k_2) \hat{B}_{\ell'_1\ell'_2L'}^{m'-m'_0}(k'_1, k'_2) \rangle \\ \langle \hat{B}_{\ell_1\ell_2L}^{m_1m_20}(k_1, k_2) \hat{B}_{\ell'_1\ell'_2L'}^{m'_1m'_20}(k'_1, k'_2) \rangle &= \frac{N_{\ell_1\ell_2L}}{N_{\text{modes}}(k_1, k_2)} \frac{N_{\ell'_1\ell'_2L'}}{N_{\text{modes}}(k'_1, k'_2)} \\ &\quad \times \int_{k_1} \frac{d^3q_1}{(2\pi)^3} \mathcal{Y}_{\ell_1}^{m_1*}(\hat{q}_1) \int_{k_2} \frac{d^3q_2}{(2\pi)^3} \mathcal{Y}_{\ell_2}^{m_2*}(\hat{q}_2) \int_{k'_1} \frac{d^3q'_1}{(2\pi)^3} \mathcal{Y}_{\ell'_1}^{m'_1*}(\hat{q}'_1) \int_{k'_2} \frac{d^3q'_2}{(2\pi)^3} \mathcal{Y}_{\ell'_2}^{m'_2*}(\hat{q}'_2) \\ &\quad \times \int \frac{d^3q_3}{(2\pi)^3} (2\pi)^3 \delta_D(\mathbf{q}_{123}) \int \frac{d^3q'_3}{(2\pi)^3} (2\pi)^3 \delta_D(\mathbf{q}'_{123}) \langle \hat{\mathcal{B}}\hat{\mathcal{B}} \rangle \mathbb{1}(q_3) \mathbb{1}(q'_3). \end{aligned} \quad (33)$$

We substitute the Gaussian limit expression from eq. (10) for $\langle \hat{\mathcal{B}}\hat{\mathcal{B}} \rangle$ to find that the right side of eq. (34) has up to six terms. We write this as

$$\begin{aligned} \langle \hat{B}_{\ell_1\ell_2L}^{m_1m_20}(k_1, k_2) \hat{B}_{\ell'_1\ell'_2L'}^{m'_1m'_20}(k'_1, k'_2) \rangle &= \frac{1}{V} \frac{N_{\ell_1\ell_2L}}{N_{\text{modes}}(k_1, k_2)} \frac{N_{\ell'_1\ell'_2L'}}{N_{\text{modes}}(k'_1, k'_2)} \sum_{i=1}^6 \int_{k_1} \frac{d^3q_1}{(2\pi)^3} \mathcal{Y}_{\ell_1}^{m_1*}(\hat{q}_1) \int_{k_2} \frac{d^3q_2}{(2\pi)^3} \mathcal{Y}_{\ell_2}^{m_2*}(\hat{q}_2) \\ &\quad \times \int \frac{d^3q_3}{(2\pi)^3} (2\pi)^3 \delta_D(\mathbf{q}_{123}) P_g(\mathbf{q}_1) P_g(\mathbf{q}_2) P_g(\mathbf{q}_3) \times \mathcal{I}_i(\mathbf{q}_1, \mathbf{q}_2, \mathbf{q}_3), \end{aligned} \quad (34)$$

and show the integrand \mathcal{I}_i for each of the six terms in Table 1. The terms are numbered by the order in which they appear in eq. (10).

As we did for the covariance of the $B_{\ell 0}$ multipoles in Section 3, after rewriting the Dirac delta function $\delta_D(\mathbf{q}_{123})$ using eq. (21), we

\mathcal{I}_1	$=$	$\delta_{k_1 k'_1}^K \delta_{k_2 k'_2}^K$	$\mathcal{Y}_{\ell'_1}^{m'_1*}(\hat{q}_1)$	$\mathcal{Y}_{\ell'_2}^{m'_2*}(\hat{q}_2)$	$\mathbb{1}(q_3)$
\mathcal{I}_2	$=$	$\delta_{k_1 k'_1}^K$	$\mathcal{Y}_{\ell'_1}^{m'_1*}(\hat{q}_1)$		$\Pi_{k'_2}(q_3) \mathcal{Y}_{\ell'_2}^{m'_2*}(\hat{q}_3)$
\mathcal{I}_3	$=$	$\delta_{k_1 k'_2}^K$	$\mathcal{Y}_{\ell'_2}^{m'_2*}(\hat{q}_1)$		$\Pi_{k'_1}(q_3) \mathcal{Y}_{\ell'_1}^{m'_1*}(\hat{q}_3)$
\mathcal{I}_4	$=$	$\delta_{k_1 k'_2}^K \delta_{k_2 k'_1}^K$	$\mathcal{Y}_{\ell'_2}^{m'_2*}(\hat{q}_1)$	$\mathcal{Y}_{\ell'_1}^{m'_1*}(\hat{q}_2)$	$\mathbb{1}(q_3)$
\mathcal{I}_5	$=$	$\delta_{k_2 k'_1}^K$		$\mathcal{Y}_{\ell'_1}^{m'_1*}(\hat{q}_2)$	$\Pi_{k'_2}(q_3) \mathcal{Y}_{\ell'_2}^{m'_2*}(\hat{q}_3)$
\mathcal{I}_6	$=$	$\delta_{k_2 k'_2}^K$		$\mathcal{Y}_{\ell'_2}^{m'_2*}(\hat{q}_2)$	$\Pi_{k'_1}(q_3) \mathcal{Y}_{\ell'_1}^{m'_1*}(\hat{q}_3)$

Table 1. Integrands \mathcal{I}_i for each of the six terms of $\langle \hat{B}_{\ell_1 \ell_2 L}^{m_1 m_2 0}(k_1, k_2) \hat{B}_{\ell'_1 \ell'_2 L'}^{m'_1 m'_2 0}(k'_1, k'_2) \rangle$ in eq. (35). We have defined functions $\Pi_k(q)$, such that $\Pi_k(q) = 1$ if q falls into the k bin and zero otherwise, and $\mathbb{1}(k_3)$, such that $\mathbb{1}(k_3) = 1$ if k_3 falls into the allowed (k_{\min}, k_{\max}) range and zero otherwise.

can compute the covariance for the TripoSH multipoles using 3D FFTs. We found that this allowed for a relatively fast computation of the covariance matrix that also yielded an invertible covariance matrix.⁶

4.3 $B_{\ell_1 \ell_2 L}$ Fisher forecast results

The Fisher matrix is

$$\mathbf{F}_{ij} \equiv \sum_{\ell_1 \ell_2 L} \sum_{k_1 k_2} \sum_{\ell'_1 \ell'_2 L'} \sum_{k'_1 k'_2} \frac{\partial B_{\ell_1 \ell_2 L}(k_1, k_2)}{\partial \theta_i} \mathbf{C}^{-1} [B_{\ell_1 \ell_2 L}(k_1, k_2), B_{\ell'_1 \ell'_2 L'}(k'_1, k'_2)] \frac{\partial B_{\ell'_1 \ell'_2 L'}(k'_1, k'_2)}{\partial \theta_j} + \mathbf{F}_{ij}^P. \quad (36)$$

We include all even L up to $L_{\max} = 6$. For each L , in principle there are an unlimited number of (ℓ_1, ℓ_2) pairs that contribute to the bispectrum signal, that satisfy $\ell_1 + \ell_2 + L = \text{even}$ and the triangle inequality. In this work we consider all allowed pairs of (ℓ_1, ℓ_2) with $\ell_1, \ell_2 \leq \ell_{\max} = 6$. This results in a total of 40 possible (ℓ_1, ℓ_2, L) combinations.

For k_1 and k_2 , we use the same k -binning as in Section 3 for the $B_{\ell m}$ multipoles: $k_{\min} = 0.02 h \text{ Mpc}^{-1}$, $k_{\max} = 0.15 h \text{ Mpc}^{-1}$, $\Delta k = 0.01 h \text{ Mpc}^{-1}$. For a multipole with $\ell_1 \neq \ell_2$, there are 196 (k_1, k_2) bins. When $\ell_1 = \ell_2$, there are 105 (k_1, k_2) bins.

We take the most minimal data set to be B_{000} , but after that it is not obvious which multipoles to include for the most efficient multipole compression. Since we wish to find the most efficient compression, we aim to include only as many multipoles as is necessary, and not all them, as this would amount to a data vector that is 5,838 bins in length. Instead, we construct the list of sufficient multipoles as follows. After B_{000} , we choose the next multipole to be whichever one out of the remaining 39 multipoles gives the largest improvements in the forecasted constraints. For a given starting set of multipoles X , we define an improvement factor for each prospective multipole Y as

$$\prod_{i=1}^7 \frac{\sigma_{\theta_i}(X)}{\sigma_{\theta_i}(X \cup Y)}, \quad (37)$$

and we choose Y such that this factor is maximized. In this case, when $X = \{B_{000}\}$, we computed this factor for each of the 39 other remaining multipoles and found that it was largest when $Y = B_{312}$. In the next iteration, $X = \{B_{000}, B_{312}\}$ and then eq. (37) is maximised when $Y = B_{220}$. We repeat this process until the constraints do not show a significant change with the addition of any further multipoles. For each set of multipoles, we compare the resulting forecast to constraints from the full z -space bispectrum (combined with the power spectrum) to obtain the results shown in Fig. 3. We find that three multipoles, $(B_{000}, B_{312}, B_{220})$, (406 bins in total) are sufficient to recover constraints that are within 8 per cent of the full bispectrum result. Beyond this, by adding three more multipoles, $(B_{314}, B_{202}, B_{110})$, (903 bins in total), constraints are within 2 per cent of the full bispectrum result.

5 MODAL BASIS DECOMPOSITION

Finally, in this section we discuss the modal approach to compressing the redshift-space bispectrum. The modal decomposition of the bispectrum is motivated by the fact that the galaxy bispectrum should be a relatively smooth function of the triangle and its orientation. This implies that for a well-chosen set of basis functions, the modal decomposition should converge efficiently with few modes.

Previous work analysing mock halo catalogs has shown that the modal decomposition works very well to recover constraints on galaxy bias and shot noise parameters as the standard bispectrum estimator in real space, without RSD (Byun et al. 2021). This work is an extension of the modal decomposition method to redshift space, demonstrating the performance for the tree-level redshift-space bispectrum in a Fisher forecast.

⁶ We also used the thin-shell approximation to compute the covariance using SHTOOLS, not based on 3D FFTs, but this calculation was computationally very expensive and yielded a covariance matrix that experienced severe numerical issues in our implementation.

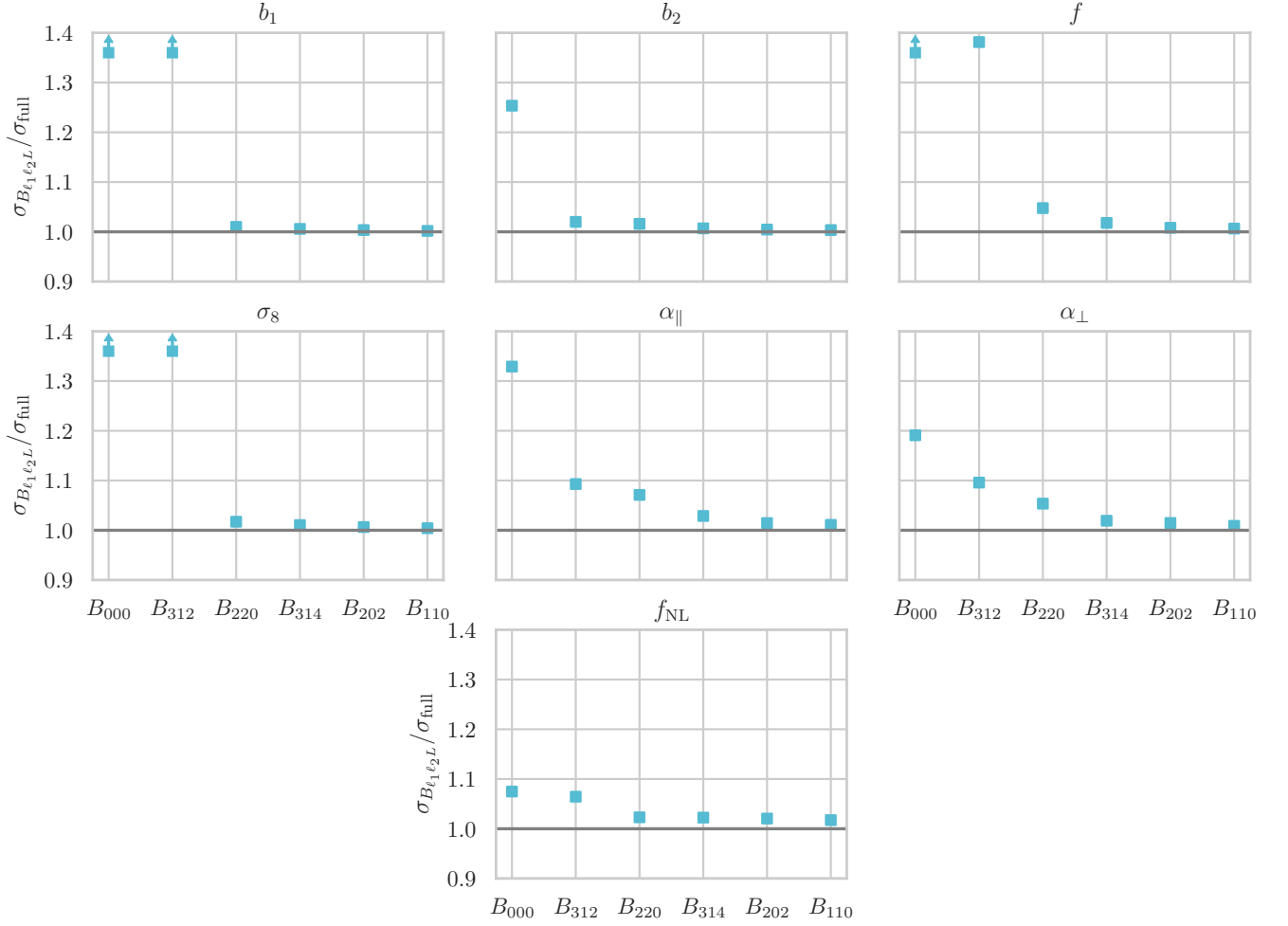


Figure 3. Forecasted constraints from $B_{\ell_1 \ell_2 L}$ including an increasing number of multipoles compared to constraints from the full redshift-space bispectrum. A value of $\sigma_{B_{\ell_1 \ell_2 L}} / \sigma_{full} = 1$ would indicate that the multipoles recover all of the available information on the parameters, $(b_1, b_2, f, \sigma_8, \alpha_{\parallel}, \alpha_{\perp}, f_{NL})$. In each panel, the leftmost point includes only B_{000} , the next point above B_{312} includes (B_{000}, B_{312}) , and so on, such that the rightmost point includes six multipoles, $(B_{000}, B_{312}, B_{220}, B_{314}, B_{202}, B_{110})$. The first three multipoles are sufficient to obtain constraints that are within 8 per cent of the full bispectrum results, while including the six multipoles shown here will obtain constraints that are within 2 per cent of the full bispectrum.

We note that the modal decomposition method is general—at its core it is simply using a separable basis to expand the bispectrum—, and what we implement in this work is one specific form that this basis may take. There are other options for basis choices that could be explored and compared, such as the modal decomposition in [Regan \(2017\)](#) that is based on Legendre multipoles.

5.1 Modal decomposition

In the modal decomposition approach, the weighted bispectrum is approximated as a linear combination of basis functions,

$$wB_g(\mathbf{k}_1, \mathbf{k}_2, \mathbf{k}_3) = \sum_{n=0}^{N_{\text{modes}}} \beta_n^Q Q_n(\mathbf{k}_1, \mathbf{k}_2, \mathbf{k}_3), \quad (38)$$

where w is a weighting function that in general depends on the three \mathbf{k}_i wave-vectors, β_n^Q are the modal expansion coefficients, and Q_n are the basis functions. If the basis functions are chosen such that only relatively small N_{modes} is necessary to reconstruct B to sufficient accuracy, then the modal compression would be very efficient.

To solve for the modal coefficients given a model for B , we first define the inner product,

$$\langle\langle X|Y \rangle\rangle \equiv \int_{\mathbf{k}_1} \int_{\mathbf{k}_2} \int_{\mathbf{k}_3} (2\pi)^3 \delta_D(\mathbf{k}_{123}) \frac{X(\mathbf{k}_1, \mathbf{k}_2, \mathbf{k}_3) Y(\mathbf{k}_1, \mathbf{k}_2, \mathbf{k}_3)}{k_1 k_2 k_3}, \quad (39)$$

which integrates the product of two functions over all triangle shapes and orientations. Then we can solve the linear equation

$$\langle\langle wB|Q \rangle\rangle = \tilde{\beta}^Q \cdot \gamma \quad (40)$$

n	$q_n(k, \mu)$	n	$q_n(k, \mu)$	n	$q_n(k, \mu)$	n	$q_n(k, \mu)$
0	1	6	μ^2	12	$P_m(k)\mu/k$	18	$P_m(k)/k^2\mathcal{M}(k)$
1	$P_m(k)$	7	$P_m(k)\mu^2$	13	$P_m(k)\mu^3/k$	19	$P_m(k)\mu^2/\mathcal{M}(k)$
2	$P_m(k)k^2$	8	$P_m(k)\mu^2k^2$	14	$P_m(k)\mu^4$	20	$P_m(k)\mu^2k^2/\mathcal{M}(k)$
3	$P_m(k)/k^2$	9	$P_m(k)\mu^2/k^2$	15	μk	21	$P_m(k)\mu/k\mathcal{M}(k)$
4	k^2	10	μ^2k^2	16	$P_m(k)/\mathcal{M}(k)$	22	$\mathcal{M}(k)$
5	k^4	11	μ^2k^4	17	$P_m(k)k^2/\mathcal{M}(k)$	23	$\mu^2\mathcal{M}(k)$

Table 2. Set of 24 $q_n(k, \mu)$ functions for recovering the tree-level bispectrum. $P_m(k)$ is the linear matter power spectrum. $\mathcal{M}(k)$ depends on the matter transfer function and is defined in Section 2.1.

to obtain the β_n^Q , where we have defined the positive-definite symmetric matrix $\gamma \equiv \langle\langle Q|Q \rangle\rangle$.

This modal decomposition method so far applies generally in real space and redshift space. Compared to previous work in real space (e.g. Byun et al. (2021)), the optimal weighting in redshift space is different,

$$w \equiv \frac{\sqrt{k_1 k_2 k_3}}{\sqrt{P_g(k_1)P_g(k_2)P_g(k_3)}}, \quad (41)$$

and it will be necessary to choose our Q_n basis functions to have an angular dependence so that the anisotropic component of the bispectrum, induced by RSD and AP effects, can be captured efficiently by the modal expansion.

5.2 Custom modes

While the Q_n basis functions can in principle be constructed from any set of basis functions, in previous work on the real-space modal bispectrum, it was advantageous to build a basis of separable *custom modes* that were functions that could analytically reproduce the tree-level bispectrum model exactly (Hung et al. 2019a; Byun et al. 2021). We apply the same approach here to the redshift-space bispectrum.

The tree-level redshift-space bispectrum expression in eq. (2) can be rewritten exactly as a sum of 83 separable Q_n basis functions,⁷ where each Q_n is made up of a combination of three $q_n(k, \mu)$ functions from Table 2,

$$Q_n(k_1, k_2, k_3, \mu_1, \mu_2, \mu_3) = q_{\{p\}}(k_1, \mu_1) q_{\{r\}}(k_2, \mu_2) q_{\{s\}}(k_3, \mu_3). \quad (42)$$

The curly brackets around the p , r , and s subscripts signify that the function is symmetrized over permutations of p , r and s . We refer to this basis of Q_n functions as *custom modes*. For compactness, we will sort basis functions based on increasing values of $p + r + s$. Then the first five (p, r, s) combinations are (0, 0, 0), (0, 0, 1), (0, 1, 1), (0, 2, 3), (0, 0, 7) and the last five combinations are (16, 16, 23), (16, 19, 22), (16, 19, 23), (19, 19, 22), (19, 19, 23).

In the case where the AP parameters are fixed to unity, $\alpha_{\parallel} = \alpha_{\perp} = 1$, it is straightforward to derive the corresponding coefficients β_n^Q for this basis, given the parameters of interest in this work: $b_1, b_2, f, \sigma_8, \alpha_{\parallel}, \alpha_{\perp}$, and f_{NL} . However, when the AP parameters are varied, the shape of the bispectrum changes in a way that may or may not be well-described by the existing set of 83 custom modes. Hence we also consider a larger basis of *extended custom modes* which includes additional modes defined to capture the changes to the custom Q_n induced by the AP parameters. Therefore, the extended custom basis consists of 83 custom modes, 82 functions for $\partial_{\alpha_{\parallel}} Q_n$, and 82 functions for $\partial_{\alpha_{\perp}} Q_n$, for a total of 247 basis functions. There are only 82 derivative functions for each AP parameter, because one of the custom Q_n is a constant (when $p = r = s = 0$), so its derivative with respect to the AP parameters is zero.

For each choice of basis, the custom modes and extended custom modes, we use FFTs to calculate the γ matrix consisting of inner products between all pairs of Q_n , in the same manner as in Byun et al. (2021).

5.3 Orthonormal modes and covariance

The advantage of the Q_n basis is that given input parameters, $(b_1, b_2, f, \sigma_8, \alpha_{\parallel}, \alpha_{\perp}, f_{\text{NL}})$, we can analytically predict the β_n^Q expansion coefficients. On the other hand, it is also convenient to rotate to another basis where the basis functions are orthogonal, so that the expansion coefficients on this basis are uncorrelated. We will use a set of orthonormal basis functions called R_n which is defined by having $\langle\langle R_n | R_m \rangle\rangle = \delta_{nm}^K$. On this basis then,

$$\beta_n^R = \langle\langle wB | R_n \rangle\rangle, \quad (43)$$

and to rotate expansion coefficients from the β_n^Q to the β_n^R is

$$\beta_n^R = \lambda^T \beta_n^Q, \quad (44)$$

where λ is the lower-triangular matrix that results from the Cholesky decomposition of γ , $\gamma = \lambda \lambda^T$.

⁷ We note that if we fix $f_{\text{NL}} = 0$ in the modeling, then only 38 Q_n are necessary to recover eq. (2).

5.4 Modal estimator and covariance

From eq. (40), the estimator for the orthonormal modal coefficients is

$$\beta_n^R = \langle w\mathcal{B}|R_n \rangle, \quad (45)$$

and the covariance is

$$\begin{aligned} \langle \beta_n^R \beta_m^R \rangle &= \int \frac{d^3 k_1}{(2\pi)^3} \int \frac{d^3 k_2}{(2\pi)^3} \int \frac{d^3 k_3}{(2\pi)^3} (2\pi)^3 \delta_D(\mathbf{k}_{123}) \frac{wR_n(\mathbf{k}_1, \mathbf{k}_2, \mathbf{k}_3)}{k_1 k_2 k_3} \\ &\quad \times \int \frac{d^3 k'_1}{(2\pi)^3} \int \frac{d^3 k'_2}{(2\pi)^3} \int \frac{d^3 k'_3}{(2\pi)^3} (2\pi)^3 \delta_D(\mathbf{k}'_{123}) \frac{wR_m(\mathbf{k}'_1, \mathbf{k}'_2, \mathbf{k}'_3)}{k'_1 k'_2 k'_3} \langle \mathcal{B}(\mathbf{k}_1, \mathbf{k}_2, \mathbf{k}_3) \mathcal{B}(\mathbf{k}'_1, \mathbf{k}'_2, \mathbf{k}'_3) \rangle. \end{aligned} \quad (46)$$

Using eq. (10) for $\langle \mathcal{B}\mathcal{B}' \rangle$, the Gaussian covariance matrix for β_n^R simplifies to

$$\langle \beta_n^R \beta_m^R \rangle = \frac{6}{V} \delta_{nm}^K. \quad (47)$$

5.5 Note on computing derivatives with respect to AP parameters

Unlike the other parameters ($b_1, b_2, f, \sigma_8, f_{\text{NL}}$), the effect of the AP parameters ($\alpha_{\parallel}, \alpha_{\perp}$) on the the custom β^Q coefficients is not trivial to write down analytically because the AP parameters distort the k -dependent shape of the bispectrum. For general values of the AP parameters, we can still compute the tree-level bispectrum *exactly* as

$$\tilde{B}_{\text{tree}}(\mathbf{k}, \mathbf{k}_2, \mathbf{k}_3, \alpha) = \sum_{n=0}^{82} \tilde{\beta}_n^Q \tilde{Q}_n(\mathbf{k}_1, \mathbf{k}_2, \mathbf{k}_3, \alpha). \quad (48)$$

Here, each \tilde{Q}_n has the same functional form as the custom modes, Q_n , but the arguments are now wave-vectors that are rescaled by the AP parameters. Correspondingly, $\tilde{\beta}_n^Q$ have the same dependence on the input parameters ($b_1, b_2, f, \sigma_8, f_{\text{NL}}$) as before, but now they are additionally divided by the appropriate AP factors, $\tilde{\beta}_n^Q = \beta_n^Q / (\alpha_{\parallel} \alpha_{\perp}^2)^2$.

We would like to find the modal coefficients β^Q that can reconstruct this \tilde{B}_{tree} ,

$$w(\mathbf{k}) \tilde{B}_{\text{tree}}(\mathbf{k}, \alpha) = \sum_m \beta_m^Q Q_m(\mathbf{k}). \quad (49)$$

Combining eqs. (48) and (49), we find β^Q by solving the linear equation

$$\gamma \cdot \beta^Q = \langle Q|w\tilde{Q} \rangle \cdot \tilde{\beta}^Q. \quad (50)$$

While the custom modes can reconstruct the fiducial bispectrum with $\alpha_{\parallel} = \alpha_{\perp} = 1$ exactly, we do not know *a priori* whether they are efficient at capturing changes to the bispectrum induced by varying the AP parameters.

5.6 Fisher forecast results

The Fisher matrix is

$$\begin{aligned} \mathbf{F}_{ij} &\equiv \sum_{nm} \frac{\partial \beta_n^R}{\partial \theta_i} \mathbf{C}^{-1} [\beta_n^R, \beta_m^R] \frac{\partial \beta_m^R}{\partial \theta_j} + \mathbf{F}_{ij}^P \\ &= \frac{V}{6} \sum_n \frac{\partial \beta_n^R}{\partial \theta_i} \frac{\partial \beta_n^R}{\partial \theta_j} + \mathbf{F}_{ij}^P. \end{aligned} \quad (51)$$

The comparison of constraints from the modal bispectrum vs the full redshift-space bispectrum is shown in Fig. 4 as a function of the number of modes included. We show the results for both the custom modes and the extended custom modes. To show the most efficient compression, we order the modes in the same way that we ordered the $B_{\ell_1 \ell_2 L}$ multipoles in Section 4.3. The most minimal set of modes requires at least 7, since we are forecasting constraints for 7 parameters, and we choose these starting modes to be the 7 modes with the smallest $p + r + s$ values.

We find that using only the original set of 83 custom modes (light blue circles in Fig. 4), the modal constraints do not converge to within 10 per cent of the constraints from the full bispectrum. This is because the AP parameters change the bispectrum's dependence on triangles and orientations in a way that is not captured by the custom modes, but this issue is resolved when the extended custom modes are used (dark blue circles). In this case, only 14 modes are necessary to recover constraints that are within 10 per cent of the full bispectrum result, and only 42 modes are required to obtain constraints that are within 2 per cent. Within the set of the $N_{\text{modes}} = 14$ modes, the fact that two of these are from the extended custom basis (and not included in the original 83 custom modes) is what allows the constraints from the extended basis to recover constraints that are closer to what is obtained from the full bispectrum. Similarly, within the set of $N_{\text{modes}} = 42$ modes, 10 of these are only in the extended basis.

We emphasise that the extended custom modes are only necessary if we are interested in constraining the AP factors. Performing the same forecast as above, except including only the parameters ($b_1, b_2, f, \sigma_8, f_{\text{NL}}$), we find that a basis of only 13 of the original (non-extended) custom modes is sufficient to obtain forecasted errors that are within 2 per cent of the full bispectrum result.

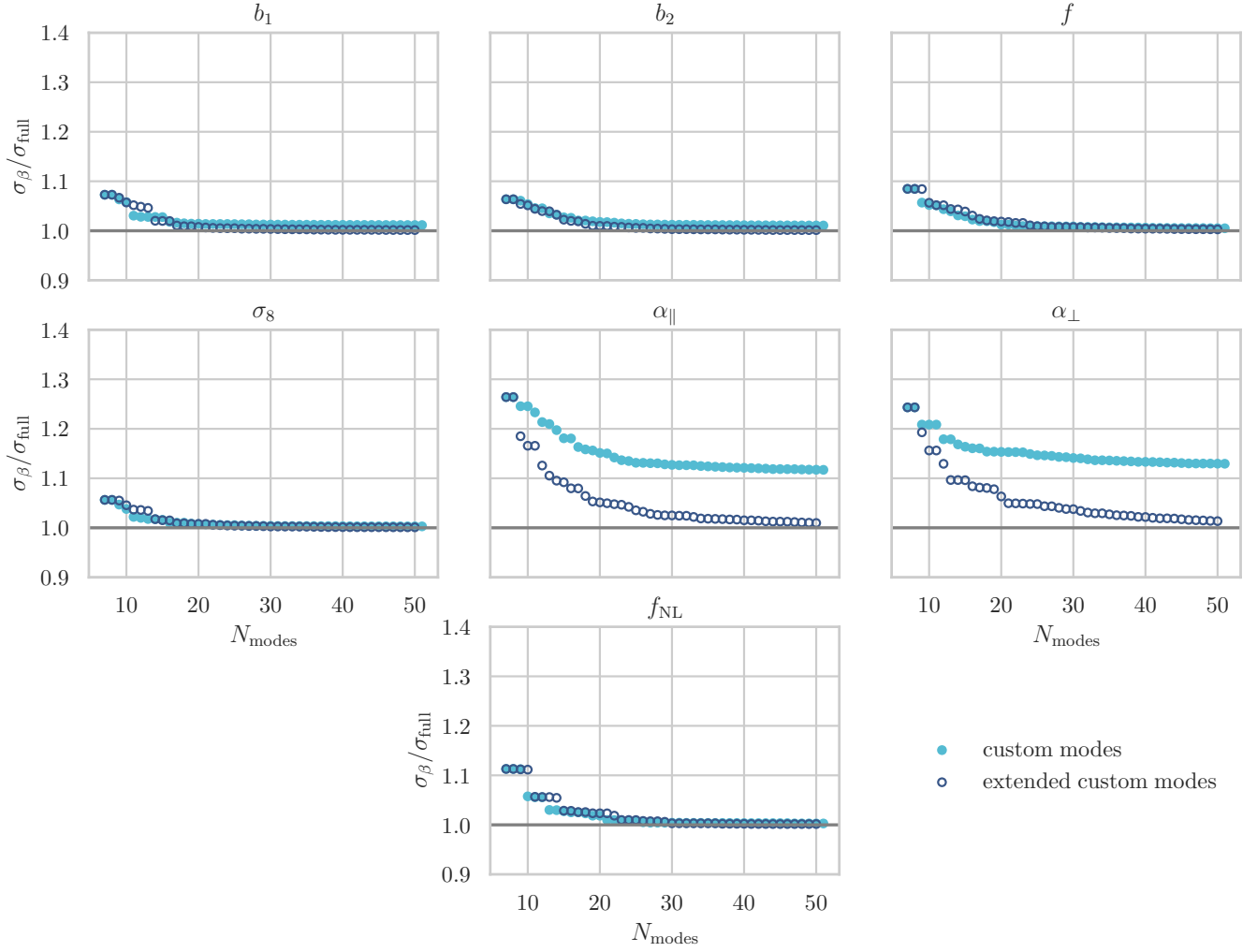


Figure 4. Forecasted constraints from the modal decomposition of the bispectrum including an increasing number of basis functions, N_{modes} , compared to constraints from the full redshift-space bispectrum. The basis of custom modes (filled light blue circles) are not sufficient to recover constraints on the AP parameters to within 10 per cent of the full bispectrum constraint. However, the basis of extended custom modes (empty dark blue circles) requires only 14 modes to recover constraints to within 10 per cent or 42 modes to recover constraints to within 2 per cent, of the full bispectrum.

6 DISCUSSION

In this work, we extended the modal decomposition method to the redshift-space bispectrum and compared its performance and efficiency with two multipole decompositions in the literature: the spherical harmonic $B_{\ell m}(k_1, k_2, k_3)$ multipoles (Soccimarro 2015) and the tripolar spherical harmonic $B_{\ell_1 \ell_2 L}(k_1, k_2)$ multipoles (Sugiyama et al. 2019). We compared these three bispectrum compression schemes by computing Fisher forecasted constraints on a basic set of cosmological and galaxy bias parameters, $(b_1, b_2, f, \sigma_8, \alpha_{\parallel}, \alpha_{\perp}, f_{\text{NL}})$, for a reference survey. In each case, we compared the constraint from the compressed statistic to the constraint from the full redshift-space bispectrum. We find that the modal bispectrum can recover the same forecasted constraining power as the full bispectrum to within 10 (2) per cent by using 14 (42) modal expansion coefficients. A comparable level of agreement can also be achieved in our forecasts for the other multipole decompositions, $B_{\ell m}$ and $B_{\ell_1 \ell_2 L}$, through using a much larger data vector. This is illustrated for one of the parameters, α_{\parallel} , in Fig. 5. We have chosen to show the comparison between estimators for this particular parameter, because this is the parameter that typically required more multipoles or modes for constraints to converge.

Further development of the modal decomposition approach for the galaxy bispectrum could take different directions. As this work is based on a tree-level bispectrum model, it remains to be tested with simulations or mock catalogs how well the bases considered here could reconstruct the non-linear matter or galaxy bispectrum. Furthermore, as current and future galaxy surveys observe larger areas of the sky, it will become necessary to move beyond bispectrum estimators based on the global plane parallel approximation, considered in this work. This has been explored for the $B_{\ell m}$ and $B_{\ell_1 \ell_2 L}$ multipoles in Soccimarro (2015) and Sugiyama et al. (2019), but we leave a corresponding modal basis to future work. Another layer of realism that needs to be included in future is how the survey window function is incorporated in the modeling

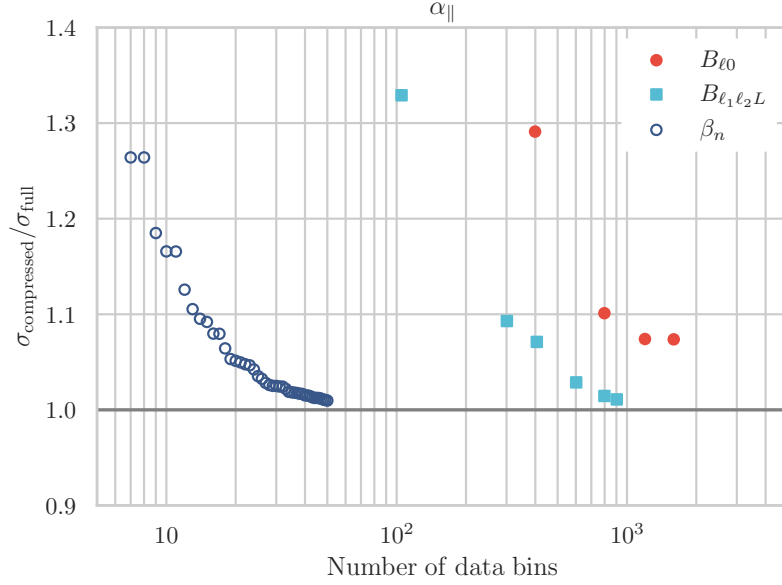


Figure 5. Per cent difference between the forecasted constraint on the AP parameter, α_{\parallel} , from the $B_{\ell 0}$ multipoles (red circles), TripoSH $B_{\ell_1 \ell_2 L}$ multipoles (light blue squares), and modal coefficients β_n (empty dark blue circles) compared to the forecasted constraint from the full redshift-space bispectrum, σ_{full} . The data shown here are the same as the data shown in the α_{\parallel} panels of Figs. 2, 3, and 4, except here the x -axis is the number of data bins that are used in the forecast to obtain $\sigma_{\text{compressed}}$. While all three compression schemes can recover constraints that are within 10 per cent of the full bispectrum constraint, this figure shows that the modal decomposition requires far fewer data bins.

of the modal coefficients. Recent work on windowless bispectrum estimation (Philcox 2021) and window function convolutions (Pardede et al. 2022) may be transferable to the modal approach as well.

ACKNOWLEDGEMENTS

JB would like to thank Chen Heinrich for helpful discussions and code comparisons. We acknowledge support from the SPHEREx project under a contract from the NASA/GODDARD Space Flight Center to the California Institute of Technology. This research was also supported by the David and Lucile Packard Foundation. Part of this work is based upon High Performance Computing (HPC) resources supported by the University of Arizona TRIF, UITS, and Research, Innovation, and Impact (RII) and maintained by the UArizona Research Technologies department.

DATA AVAILABILITY

The data underlying this article will be shared on reasonable request to the corresponding author.

REFERENCES

- Ade P., et al., 2014, *Astron. Astrophys.*, 571, A24
 Ade P. A. R., et al., 2016, *Astron. Astrophys.*, 594, A16
 Agarwal N., Desjacques V., Jeong D., Schmidt F., 2021, *JCAP*, 03, 021
 Aghamousa A., et al., 2016
 Aghanim N., et al., 2020, *Astron. Astrophys.*, 641, A6
 Alcock C., Paczynski B., 1979, *Nature*, 281, 358
 Alsing J., Wandelt B., 2018, *Mon. Not. Roy. Astron. Soc.*, 476, L60
 Baldauf T., Seljak U., Desjacques V., McDonald P., 2012, *Phys. Rev. D*, 86, 083540
 Barreira A., 2021
 Bernardeau F., Colombi S., Gaztanaga E., Scoccimarro R., 2002, *Phys. Rept.*, 367, 1
 Blanchard A., et al., 2020, *Astron. Astrophys.*, 642, A191
 Blas D., Lesgourgues J., Tram T., 2011, *JCAP*, 07, 034
 Bose B., Taruya A., 2018, *JCAP*, 10, 019
 Bose B., Byun J., Lacasa F., Moradinezhad Dizgah A., Lombriser L., 2020, *JCAP*, 02, 025
 Byun J., Eggemeier A., Regan D., Seery D., Smith R. E., 2017, *Mon. Not. Roy. Astron. Soc.*, 471, 1581

- Byun J., Franco F. O., Howlett C., Bonvin C., Obreschkow D., 2020, *Mon. Not. Roy. Astron. Soc.*, 497, 1765
- Byun J., Oddo A., Porciani C., Sefusatti E., 2021, *JCAP*, 03, 105
- Cabass G., Ivanov M. M., Philcox O. H. E., Simonović M., Zaldarriaga M., 2022a
- Cabass G., Ivanov M. M., Philcox O. H. E., Simonović M., Zaldarriaga M., 2022b
- Chan K. C., Scoccimarro R., Sheth R. K., 2012, *Phys. Rev. D*, 85, 083509
- Chartier N., Wandelt B. D., 2021, *Mon. Not. Roy. Astron. Soc.*, 509, 2220
- Chiang C.-T., Wagner C., Schmidt F., Komatsu E., 2014, *JCAP*, 05, 048
- Chiang C.-T., Wagner C., Sánchez A. G., Schmidt F., Komatsu E., 2015, *JCAP*, 09, 028
- Clarkson C., de Weerd E. M., Jolicoeur S., Maartens R., Umeh O., 2019, *Mon. Not. Roy. Astron. Soc.*, 486, L101
- Colavincenzo M., et al., 2019, *Mon. Not. Roy. Astron. Soc.*, 482, 4883
- Dai J.-P., Verde L., Xia J.-Q., 2020, *JCAP*, 08, 007
- Doré O., et al., 2014
- Eggemeier A., Smith R. E., 2017, *Mon. Not. Roy. Astron. Soc.*, 466, 2496
- Fergusson J., Liguori M., Shellard E., 2010, *Phys. Rev. D*, 82, 023502
- Fergusson J., Liguori M., Shellard E., 2012a, *JCAP*, 12, 032
- Fergusson J. R., Regan D. M., Shellard E. P. S., 2012b, *Phys. Rev.*, D86, 063511
- Franco F. O., Bonvin C., Obreschkow D., Ali K., Byun J., 2019, *Phys. Rev.*, D99, 103530
- Friedrich O., Eifler T., 2018, *Mon. Not. Roy. Astron. Soc.*, 473, 4150
- Gagrani P., Samushia L., 2017, *Mon. Not. Roy. Astron. Soc.*, 467, 928
- Gil-Marín H., Noreña J., Verde L., Percival W. J., Wagner C., Manera M., Schneider D. P., 2015a, *Mon. Not. Roy. Astron. Soc.*, 451, 539
- Gil-Marín H., et al., 2015b, *Mon. Not. Roy. Astron. Soc.*, 452, 1914
- Gil-Marín H., Percival W. J., Verde L., Brownstein J. R., Chuang C.-H., Kitaura F.-S., Rodríguez-Torres S. A., Olmstead M. D., 2017, *Mon. Not. Roy. Astron. Soc.*, 465, 1757
- Gualdi D., Verde L., 2020, *JCAP*, 06, 041
- Gualdi D., Verde L., 2022
- Gualdi D., Manera M., Joachimi B., Lahav O., 2018, *Mon. Not. Roy. Astron. Soc.*, 476, 4045
- Gualdi D., Gil-Marín H., Manera M., Joachimi B., Lahav O., 2019a, *Mon. Not. Roy. Astron. Soc.*, 484, L29
- Gualdi D., Gil-Marín H., Schuhmann R. L., Manera M., Joachimi B., Lahav O., 2019b, *Mon. Not. Roy. Astron. Soc.*, 484, 3713
- Gualdi D., Gil-Marín H., Manera M., Joachimi B., Lahav O., 2020, *Mon. Not. Roy. Astron. Soc.*, 497, 776
- Hahn T., 2005, *Comput. Phys. Commun.*, 168, 78
- Hahn T., 2015, *J. Phys. Conf. Ser.*, 608, 012066
- Hahn C., Villaescusa-Navarro F., 2021, *JCAP*, 04, 029
- Hahn C., Villaescusa-Navarro F., Castorina E., Scoccimarro R., 2020, *JCAP*, 03, 040
- Hajian A., Souradeep T., 2003, *Astrophys. J. Lett.*, 597, L5
- Hajian A., Souradeep T., 2005
- Hall A., Taylor A., 2019, *Mon. Not. Roy. Astron. Soc.*, 483, 189
- Heavens A., Jimenez R., Lahav O., 2000, *Mon. Not. Roy. Astron. Soc.*, 317, 965
- Hung J., Fergusson J. R., Shellard E. P. S., 2019a
- Hung J., Manera M., Shellard E., 2019b
- Joachimi B., 2017, *Mon. Not. Roy. Astron. Soc.*, 466, L83
- Karagiannis D., Lazanu A., Liguori M., Raccanelli A., Bartolo N., Verde L., 2018, *Mon. Not. Roy. Astron. Soc.*, 478, 1341
- Lazanu A., Giannantonio T., Schmittfull M., Shellard E. P. S., 2016, *Phys. Rev.*, D93, 083517
- Lazanu A., Giannantonio T., Schmittfull M., Shellard E., 2017, *Phys. Rev. D*, 95, 083511
- Lazeyras T., Wagner C., Baldauf T., Schmidt F., 2016, *JCAP*, 02, 018
- Maartens R., Jolicoeur S., Umeh O., De Weerd E. M., Clarkson C., Camera S., 2020, *JCAP*, 03, 065
- Maartens R., Jolicoeur S., Umeh O., De Weerd E. M., Clarkson C., 2021, *JCAP*, 04, 013
- Moradinezhad Dizgah A., Lee H., Schmittfull M., Dvorkin C., 2020, *JCAP*, 04, 011
- Moradinezhad Dizgah A., Biagetti M., Sefusatti E., Desjacques V., Noreña J., 2021, *JCAP*, 05, 015
- Obreschkow D., Power C., Bruderer M., Bonvin C., 2013, *Astrophys. J.*, 762, 115
- Oddo A., Rizzo F., Sefusatti E., Porciani C., Monaco P., 2021, *JCAP*, 11, 038
- Pardede K., Rizzo F., Biagetti M., Castorina E., Sefusatti E., Monaco P., 2022
- Pearson D. W., Samushia L., 2016, *Mon. Not. Roy. Astron. Soc.*, 457, 993
- Philcox O. H. E., 2021, *Phys. Rev. D*, 104, 123529
- Philcox O. H. E., Ivanov M. M., 2022, *Phys. Rev. D*, 105, 043517
- Philcox O. H. E., Ivanov M. M., Zaldarriaga M., Simonovic M., Schmittfull M., 2021, *Phys. Rev. D*, 103, 043508
- Pratten G., Munshi D., 2012, *Mon. Not. Roy. Astron. Soc.*, 423, 3209
- Regan D., 2017, *JCAP*, 12, 020
- Regan D. M., Schmittfull M. M., Shellard E. P. S., Fergusson J. R., 2012, *Phys. Rev.*, D86, 123524
- Rizzo F., Moretti C., Pardede K., Eggemeier A., Oddo A., Sefusatti E., Porciani C., Monaco P., 2022
- Ruggeri R., Castorina E., Carbone C., Sefusatti E., 2018, *JCAP*, 03, 003
- Saito S., Baldauf T., Vlah Z., Seljak U., Okumura T., McDonald P., 2014, *Phys. Rev. D*, 90, 123522
- Samushia L., Slepian Z., Villaescusa-Navarro F., 2021, *Mon. Not. Roy. Astron. Soc.*, 505, 628
- Schmittfull M., Moradinezhad Dizgah A., 2021, *JCAP*, 03, 020
- Schmittfull M. M., Regan D. M., Shellard E. P. S., 2013, *Phys. Rev.*, D88, 063512
- Schmittfull M., Baldauf T., Seljak U., 2015, *Phys. Rev. D*, 91, 043530
- Scoccimarro R., 2015, *Phys. Rev. D*, 92, 083532
- Scoccimarro R., Couchman H. M. P., Frieman J. A., 1999, *Astrophys. J.*, 517, 531
- Sefusatti E., Crocce M., Pueblas S., Scoccimarro R., 2006, *Phys. Rev. D*, 74, 023522

- Shiraishi M., Sugiyama N. S., Okumura T., 2017, *Phys. Rev. D*, 95, 063508
- Slepian Z., et al., 2017, *Mon. Not. Roy. Astron. Soc.*, 468, 1070
- Song Y.-S., Taruya A., Oka A., 2015, *JCAP*, 08, 007
- Sugiyama N. S., Shiraishi M., Okumura T., 2018, *Mon. Not. Roy. Astron. Soc.*, 473, 2737
- Sugiyama N. S., Saito S., Beutler F., Seo H.-J., 2019, *Mon. Not. Roy. Astron. Soc.*, 484, 364
- Sugiyama N. S., Saito S., Beutler F., Seo H.-J., 2020, *Mon. Not. Roy. Astron. Soc.*, 497, 1684
- Szapudi I., 2004, *Astrophys. J.*, 614, 51
- Tegmark M., Taylor A. N., Heavens A. F., 1997, *Astrophys. J.*, 480, 22
- Tellarini M., Ross A. J., Tasinato G., Wands D., 2016, *JCAP*, 06, 014
- Varshalovich D. A., Moskalev A. N., Khersonskii V. K., 1988, Quantum Theory of Angular Momentum. World Scientific Publishing Co., New Jersey, USA
- Wadekar D., Scoccimarro R., 2020, *Phys. Rev. D*, 102, 123517
- Wieczorek M. A., Meschede M., 2018, *Geochemistry, Geophysics, Geosystems*, 19, 2574
- Wolstenhulme R., Bonvin C., Obreschkow D., 2015, *Astrophys. J.*, 804, 132
- Yamauchi D., Yokoyama S., Tashiro H., 2017, *Phys. Rev. D*, 96, 123516
- Yankelevich V., Porciani C., 2019, *Mon. Not. Roy. Astron. Soc.*, 483, 2078
- Yankelevich V., McCarthy I. G., Kwan J., Stafford S. G., Liu J., 2022
- de Weerd E. M., Clarkson C., Jolicœur S., Maartens R., Umeh O., 2020, *JCAP*, 05, 018

This paper has been typeset from a $\text{\TeX}/\text{\LaTeX}$ file prepared by the author.